

Durability Aspects of Fast Charging, Mechanical Constraint, and Inhomogeneity in Lithium-Ion Batteries

Abdilbari Shifa Mussa

Doctoral Thesis, 2018
KTH Royal Institute of Technology
School of Engineering Sciences in Chemistry,
Biotechnology and Health
Department of Chemical Engineering
Applied Electrochemistry
SE- 100 44 Stockholm, Sweden

© Abdilbari Shifa Mussa 2018

TRITA-CBH-FOU-2018:13
ISBN 978-91-7729-753-6

Akademisk avhandling som med tillstånd av Kungliga Tekniska Högskolan i Stockholm framlägges till offentlig granskning för avläggandet av teknologie doktorsexamen onsdagen den 09 maj kl 10.00 i sal F3, KTH, Lindstedtsvägen 26, Stockholm

To my family

ዳ.ዴ. “ምንግዘን ቲትማሪኛ?” ፣ “ምንግዘን ያስቡዮን?”

Abstract

The development of lithium-ion batteries with higher energy and power density, better safety, and lower cost has significantly contributed to the increased market share of electric vehicles (EVs) in the last decade. However, the expectations of end-users of EVs still require a continuous quest for better performance. One important end-user expectation is the ability of the battery to be charged rapidly, but the durability of lithium-ion batteries could be affected by the fast charging. Hence, detailed investigations are required to understand the extent and mechanism of the degradation for an optimized battery usage and material development.

In order to meet the high energy and power required in EVs, multiple large-format cells are connected in series and in parallel. Such a condition leads to an uneven distribution of temperature, pressure, and current in a cell or among cells that may cause locally inhomogeneous ageing and accelerate the global battery ageing. This thesis investigates the effects of charging rate, charging protocol, and external compression on battery durability. The impacts of inhomogeneities induced by cell design constraint, and uneven compression and temperature distributions are also addressed. The studies are based $\text{LiNi}_{1/3}\text{Mn}_{1/3}\text{Co}_{1/3}\text{O}_2$ /graphite cells. Cell housing for a controlled pressure and temperature application was developed. Electrochemical and material characterization techniques were used in the investigation.

The results show that fast charging at a rate equivalent to full charging in 20 minutes (3C rate) or less accelerates battery ageing. The ageing rate is less sensitive to charging rate in a longer charging time, i.e. at 2C and below, where it is determined more by factors such as the extent of full charging. In all cases, the capacity loss is limited by the cyclable lithium loss. External compression of a battery in an optimum range reduces ageing, but compression above or below the optimum range accelerates ageing. Lithium-ion batteries age non-uniformly. Cycling induces an increase in the impedance at the outer radius of curvature of a prismatic cell jellyroll, associated with a loss of contact between the current collector and the electrode coating. An unfavorable current distribution induced by uneven temperature distribution can accelerate battery ageing.

Keywords: Lithium-ion batteries; NMC(111); Graphite; Cycle ageing, Fast-charging; Inhomogeneity; Current distribution; Pressure; Curvature; Temperature.

Sammanfattning

I takt med att litiumjonbatterier det senaste decenniet har fått bättre prestanda och pris växer marknaden för elfordon (EV). Användare av elfordon har höga förväntningarna på batteriet. Förutom hög energi- och effekttäthet, ska de vara säkra och ha lång livslängd. En annan önskan är att batteriet ska tåla att laddas snabbt. Det finns dock en risk att snabbladdning accelererar batteriets åldring, vilket visar sig i kapacitetsförlust och ökat motstånd i batteriet. För att optimera användningen av batteriet och samtidigt minimera dess åldring behövs detaljerade undersökningar av omfattningen och bakomliggande mekanismer av åldring orsakad av snabbladdning.

För att möta de höga energi- och effektbehov som krävs i elfordon kopplas i regel flera storformatceller samman i serie och parallellt. En sådan konfiguration kan leda till en ojämn fördelning av temperatur, tryck och ström i cellen eller mellan celler, vilket i sin tur kan leda till att cellen eller cellerna åldras inhomogent. I avhandlingen behandlas inverkan av laddningshastighet, laddningsprotokoll och yttre tryck, liksom effekterna av ojämn fördelning av tryck och temperatur på funktion och livslängd. Studierna bygger på analyser av $\text{LiNi}_{1/3}\text{Mn}_{1/3}\text{Co}_{1/3}\text{O}_2$ /grafit-celler baserade på elektrokemiska mätningar och till viss del materialkaraktisering av cellkomponenterna. För studierna har ett cellhus för kontrollerat tryck och temperatur tagits fram och metodik för att mäta strömfördelning i parallellt kopplade celler.

Resultaten visar att snabbladdning som motsvarar full uppladdning på 20 minuter (3C hastighet) eller kortare accelererar åldringen av batteriet. Litiumplätering konstaterades vid 3C och gasbildning vid 4C. Vid längre uppladdningstid, det vill säga strömmar under 2C, påverkas åldringen mer av faktorer som laddningsnivån och laddningstid. Kapacitetsförlusten är i regel ett resultat av att tillgängligheten av cyklingsbart litium begränsas. Vidare visar resultaten att ett visst yttre tryck minskar åldrandet. Vid ett optimalt tryck runt 1,3 MPa hämmas tillväxten av passivskiktet på grafit elektroden, det så kallade SEI-skiktet, som konsumerar tillgängligt litium från elektrolyten. Ojämn åldring till följd av tryckgradienter i en cell kunde konstateras i en prismatisk cell. Det lägre trycket som förväntas där elektroden kröks resulterar i att kontaktmotståndet mellan folie och den

aktiva beläggningsen där ökar vid cykling. Slutligen visar avhandlingen att en ogynnsam strömfördelning inducerad av ojämn temperaturfördelning kan påskynda batteriets totala livslängd negativt.

Nyckelord: Litium-jonbatterier; NMC(111); Grafit; Cykel åldring, Snabbladdning; Inhomogenitet; Strömfördelning; Tryck; Krökning; Temperatur.

List of appended papers

Paper I

Fast charging effects on ageing for energy-optimized automotive NMC/graphite prismatic lithium-ion cells.

Abdilbari Shifa Mussa, Anti Liivat, Fernanda Marzano, Matilda Klett, Bertrand Philippe, Göran Lindbergh, Kristina Edström, Rakel Wreland Lindström, and Pontus Svens.

Manuscript

Paper II

Fast-charging to a partial state of charge in lithium-ion batteries: A comparative ageing study.

Abdilbari Shifa Mussa, Matilda Klett, Mårten Behm, Göran Lindbergh, and Rakel Wreland Lindström.

Journal of Energy Storage, **13** (2017) 325-333

Paper III

Effects of external pressure on the performance and ageing of single-layer lithium-ion pouch cell.

Abdilbari Shifa Mussa, Matilda Klett, Göran Lindbergh, and Rakel Wreland Lindström.

Journal of Power Sources, **385** (2018) 18-26

Paper IV

Inhomogeneous active layer contact loss in a cycled prismatic lithium-ion cell caused by the jelly-roll curvature.

Abdilbari Shifa Mussa, Göran Lindbergh, Peter Gudmundson, Matilda Klett, and Rakel Wreland Lindström.

Manuscript submitted to Journal of Energy Storage

Paper V

Lithium-ion battery performance and ageing under uneven temperature distribution.

Abdilbari Shifa Mussa, Göran Lindbergh, Matilda Klett, and Rakel Wreland Lindström.

Manuscript

I did not participate in some parts of the work in paper I. The cell cycling protocol was chosen and performed by Pontus Svens. The Scanning electron microscopy (SEM) and Energy dispersive X-ray spectroscopy (EDS) studies were performed by Carl Tengstedt and Fernanda Marzano. The X-ray

diffraction and physical characterization were performed by Anti Liivat. Fernanda Marzano and Bertrand Philippe were responsible for the X-ray photoelectron spectroscopy (XPS).

Paper II-V: I performed all the experimental work, analyzed the data, and wrote the manuscript under the supervision and guidance of the co-authors.

Paper IV. Peter Gudmundson wrote part of the discussion section.

List of abbreviations

BOL	Beginning of Life
BEV	Battery electric vehicle
CID	Current Interrupt Device
CC	Constant Current
CCCV	Constant Current- Constant Voltage
DIS	Diffusion Induced Stress
DMM	Differential Multimeter
DoD	Depth of Discharge
DVA	Differential Voltage Analysis
EIS	Electrochemical Impedance Spectroscopy
EDS	Energy Dispersive X-ray Spectroscopy
EOL	End of Life
EV	Electric Vehicle
HEV	Hybrid Electric Vehicle
HFR	High Frequency Resistance
ICA	Incremental Capacity Analysis
ICEVs	Internal Combustion Engine Vehicles
LAAM	Loss of Active Anode Material
LACM	Loss of Active Cathode Material
LIB	Lithium-Ion Batteries
LFP	Lithium iron phosphate
LMO	Lithium manganese oxide
NMC	Nickel manganese Cobalt oxide
PID	Proportional-Integral-Derivative
SEI	Solid Electrolyte Interphase
SEM	Scanning Electron Microscopy
SOC	State of charge

Table of Contents

1	Background	1
1.1	Lithium-ion battery	1
1.2	Ageing of lithium-ion batteries	5
1.2.1	Effects of fast charging	7
1.2.2	Effects of mechanical constraint	8
1.2.3	Inhomogeneous ageing	8
2	Scope of the thesis	10
3	Experimental	11
3.1	Materials	11
3.2	Test set-up	11
3.2.1	Pressure and temperature control	11
3.2.2	Current distribution	12
3.3	Ageing conditions	12
3.4	Sample location	14
3.5	Analysis techniques	15
3.5.1	SEM and EDS	15
3.5.2	Electrochemical measurements	15
3.5.2.1	Capacity measurement	15
3.5.2.2	EIS measurement	15
3.5.3	Cell voltage fitting analysis	15
4	Results and discussion	20
4.1	Effects of charging rate on ageing	20
4.1.1	Capacity fade	20
4.1.2	Comparison of fast charging and full charging	22
4.1.3	The dominant capacity fading mode	23
4.1.4	Impedance rise	25
4.1.5	Main ageing mechanisms	28
4.2	Effects of compressive pressure on ageing	31
4.2.1	Initial performance	31

4.2.2	Cycling.....	33
4.2.2.1	Capacity loss.....	33
4.2.2.2	Mechanism of capacity loss.....	35
4.3	Inhomogeneous ageing.....	36
4.3.1	Effects of jellyroll curvature.....	37
4.3.2	Effects of current distribution.....	40
4.3.2.1	Initial performance.....	40
4.3.2.2	Cycling.....	43
5	Conclusions and outlook.....	48
6	Acknowledgements.....	51
7	References.....	52

1 Background

The introduction of a commercial lithium-ion battery by the Sony Corporation in 1991 was a technology breakthrough that made several personal electronic devices portable and powerful [1]. It has now become an indispensable part of our daily lives, powering smartphones, tablets, and laptops among other personal electronics. Beyond the microelectronic application; the concern for environmental sustainability, energy independence, and perceived shortage of oil has significantly increased the interest in lithium-ion batteries in large-scale applications such as in electric vehicles (EVs) [1-3]. The lithium-ion battery is preferred over the other types of rechargeable batteries, including lead-acid, nickel-metal hydride, and nickel-cadmium due to its superiority in energy density, power density, and lifetime [4]. However, the performance required by the end-users is still demanding and interrelated in terms of charging time, durability, safety, and cost [5]. One important requirement is that users of EVs expect comfort in terms of 'refueling' time similar to that in the internal combustion engine vehicles (ICEV) [5-8]. As a partial solution, fast-charging can be utilized to shorten the battery charging time [7, 8], but it may accelerate battery degradation [8, 9]. The degradation may have both chemical and mechanical origins [10-17]. Furthermore, the interconnection of multiple cells in a series and parallel configuration to meet the high energy and power demand of EVs may affect the battery durability due to the non-uniform distribution of temperature, current, and mechanical constraint [18-26]. Since the battery is the most expensive single component in an electric vehicle, the premature degradation of the battery greatly affects the lifetime cost. Hence, there is a need to investigate and mitigate the degradation in order to build a durable battery and meet the end-user expectations. This thesis addresses the electrochemical, mechanical and inhomogeneous degradation issues during fast charging.

1.1 Lithium-ion battery

The lithium-ion battery is a rechargeable battery, the principle of which is that lithium ions are shuttled internally between two electrodes while electrons are transported through the external circuit and do the electrical

work, as depicted in Fig. 1.1. The electrodes are commonly intercalating porous electrodes which in an ideal case reversibly store lithium in their structure. The electrode at the higher electrochemical potential is called the positive electrode and the other at the lower potential is called the negative electrode. An electrolyte is used as a medium of transport for the lithium ions between the electrodes. A separator that allows ion transport is used to prevent physical contact between the electrodes. During charging, lithium ions are transported from the positive electrode to the negative electrode through the electrolyte and separator while electrons move in the same direction through the external circuit. The reverse process occurs during discharging, and the overall electrochemical reaction in a cell consisting of a nickel-manganese-cobalt-oxide (111) positive electrode and a graphite negative electrode is shown by equation 1.1.

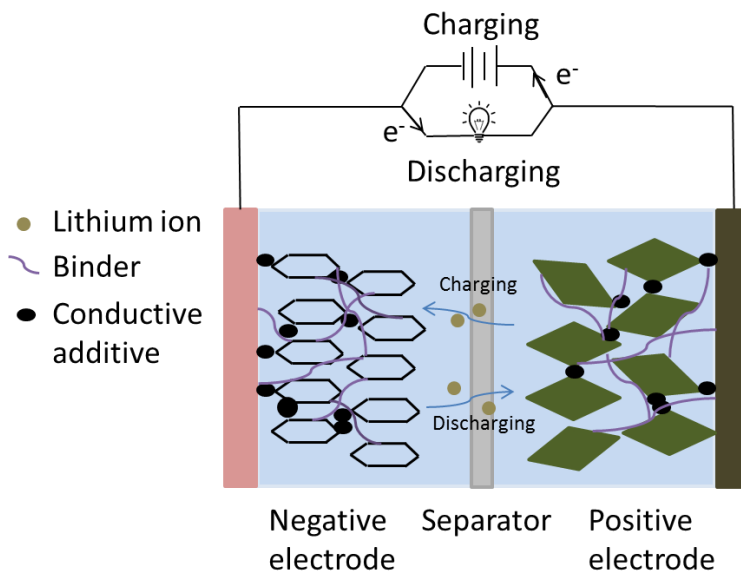
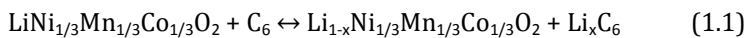


Fig. 1.1 Schematic diagram of a lithium-ion battery



The source of lithium in a commercial lithium-ion battery is commonly the positive electrode, which is also called the cathode during discharge. It is

based on different transition metal chemistries such as phosphates (ex. LiFePO_4 (LFP)) and oxides (LiCoO_2 (LCO), $\text{LiNi}_x\text{Mn}_y\text{Co}_{1-x-y}\text{O}_2$ (NMC), LiMn_2O_4 (LMO), and $\text{LiNi}_{0.80}\text{Co}_{0.15}\text{Al}_{0.05}$ (NCA)) [27, 28]. The chemistry of the positive electrode influences the performance characteristics of the battery, including the energy density, power density, thermal stability, and cycle life. Currently, NMC is the material of choice with an increasing demand by the industry because of its good combination of the performance characteristics [29]. It is available in different compositions where the widely used ones have Ni:Mn:Co ratios of 3:3:3 and 5:3:2 [29]. Graphite is the most commonly used active material in the negative electrode and present in commercial lithium-ion batteries.

The electrodes contain conductive additive and binder materials in addition to the active electrode materials. A conductive carbon is added to enhance the electronic conductivity, and a binder material (e.g. polyvinylidene fluoride (PVDF)) is used to hold the different components together and make the composite electrode mechanically stable. The electrolyte consists of a lithium salt, commonly lithium hexafluorophosphate (LiPF_6), dissolved in a mixture of organic solvents such as ethylene carbonate (EC) and diethyl carbonate (DEC).

The electrodes are produced by mixing the active material, binder, and conductive additive in a solvent (typically N-methyl pyrrolidone) and coating the mixture onto aluminum and copper foils to make the positive and negative electrodes, respectively. The electrode is dried, calendered and sliced before cell assembly. Calendering is performed by pressing the coated electrode at high pressure in order to increase the contact between the different electrode components and to control its physical properties such as porosity and tortuosity. The electrodes, together with the sandwiched separator, are spirally wound to form cylindrical cells, elliptically wound to form prismatic cells, or stacked to form pouch cells. Examples of the different cell formats are shown in Fig. 1.2. The type of cell format influences its mechanical, thermal and safety performance. The important performance characteristics are compared in Table 1.1.

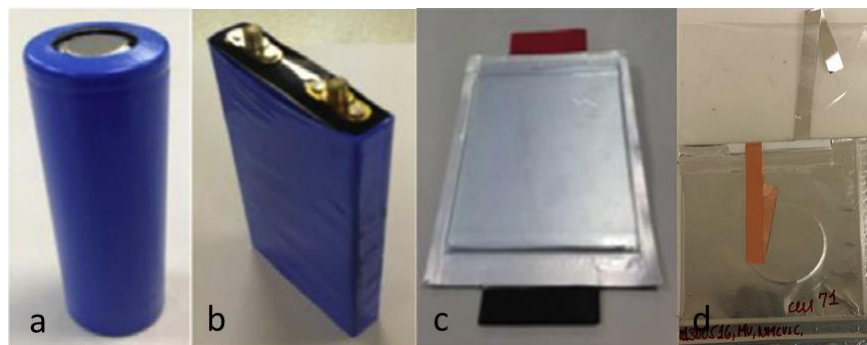


Fig. 1.2 Cell formats: a) Cylindrical b) Prismatic c) Multi-layer pouch d) single-layer pouch coin cell [30].

Table 1.1 Comparison of cell formats [30, 31]

	Cylindrical	Prismatic	Pouch
Shape	Contained in hard metal casing	Contained in hard metal casing or semi-hard casing	Contained in polymer coated metal foil pouch
Resistance against expansion	Excellent	Requires compressive plates at the ends	Requires compressive plates at the ends
Distribution of pressure on the electrode	Comparatively uniform	Non-uniform	Non-uniform
Resistance to delamination	Very good	Possible delamination	Possible delamination
Maintaining compressive pressure	Excellent	Poor	Extremely poor
Heat dissipation	Poor	Fair	Good
Safety devices	Yes	Yes	No

The hard metal casings of the cylindrical and prismatic cells provide a solid structure that protects it from venting due to internal gas pressure build-up

before activation of the safety devices [32]. The pouch cell lacks this safety feature and makes it vulnerable to venting in the presence of excessive gas evolution inside the cell [32]. Even if a hard metal casing is used in the prismatic cell, its elliptical shape makes it weaker than the cylindrical cell, and external compressive plates on either side of the cell are therefore commonly used to inhibit cell expansion [33]. The pouch cell is the weakest in terms of mechanical strength, and compressive plates are used as in the prismatic cell [31]. The application of external compression in prismatic and pouch cells makes it difficult to maintain a uniform pressure [30, 33], and the elliptic shape of the prismatic cell causes non-uniform pressure to develop between the winding curvature and the flat regions [33, 34].

The available surface-area-to-volume ratio of the cell format determines the rate of heat dissipation [32, 35]. It is poorer in the cylindrical cell than in the prismatic and pouch cells [30, 32], and it strongly influences the temperature distribution. In a cell with poor heat dissipation, the temperature at the core can be significantly higher than the skin temperature. A wide range of temperature differences in a single cell has been reported previously [35-39]. Furthermore, in large scale applications such as EVs where several cells are connected in a series and parallel configuration to meet the power and energy demand, a non-uniform temperature distribution can develop between the cells in addition to that which exists in a single cell [40-43]. The design of a single cell and its interconnection with the other cells can affect the cycle performance of the cell or the pack as a whole [44].

1.2 Ageing of lithium-ion batteries

The performance of lithium-ion batteries deteriorate over time whether they are used or not [10]. Ageing with and without use are called cycle ageing and calendar ageing, respectively. The two main consequences of ageing are energy and power fade [33]. In an electric vehicle application, for instance, the energy determines the maximum distance the vehicle can travel on a single charge, and the power determines the maximum acceleration the vehicle can achieve. Energy fading can be caused by a loss of battery capacity or in the rise of the impedance [33]. Loss of the cyclable lithium or deactivation of the active electrode material are the primary sources of capacity fade [10]. The rise in impedance is caused by the

chemical or physical transformation of the various materials and interfaces. A rise in impedance then leads to a power fade in addition to an energy fade. Generally, both energy and power fades occur at the same time and their relative importance depends on the particular application [33]. For instance, energy fade is more important than power fade in a battery electric vehicle (BEV).

Conditions such as temperature, average state of charge (SOC), depth of discharge (DOD), charge-discharge rate, and external mechanical load determine the rate of ageing [10, 45, 46]. Additionally, in a large-format cell or in cells connected in a series and parallel configuration, the inhomogeneous distribution of the ageing conditions that develops due to cycling can cause a local inhomogeneous degradation that may accelerate the overall battery ageing [21, 47, 48]. Ageing is a complex phenomenon since different conditions can interact to create different types of ageing mechanism.

Several types of ageing mechanism in a lithium-ion battery have been reported in the literature [10, 12, 14, 17, 49]. They can be either chemical or mechanical in nature. The mechanisms are different on the positive electrode and on the negative electrode side. On the negative electrode side, the most important ageing mechanism is the growth of a solid electrolyte interphase (SEI) that consumes the cyclable lithium [10, 14]. This interphase layer between the graphite and electrolyte forms because the working potential of the graphite surface is outside the stability window of the commonly used carbonate-based electrolytes [50, 51]. Normally, formation cycling is performed in a lithium-ion battery after cell construction where the initial SEI is formed [51], but continuous cycling causes the graphite particles to expand and form cracks in the SEI layer, exposing new surface for further SEI growth. The SEI growth decreases in rate with time, but it continues throughout the lifetime of the battery and consumes the cyclable lithium [51]. Other ageing mechanisms in the graphite include graphite exfoliation, lithium plating, gas evolution, current collector corrosion, and electrode layer delamination [14]. Various types of ageing mechanism have been reported on the positive electrode side [10, 16, 17]. A very thin resistive layer of the electrolyte oxidation product forms on the surface of the electrode, contributing to the rise in cell impedance.

Particles can crack due to a diffusion-induced stress (DIS) developed as a result of an inhomogeneous lithium concentration in the particles or in the electrode. Transition metals can dissolve from the positive electrode and be deposited on the SEI of the graphite electrode, making the SEI layer more conductive and accelerating the loss of the cyclable lithium as a result. Structural disordering and phase change both on the surface and in the bulk of the electrode has also been reported [16]. Another important mechanism at the positive electrode is gas evolution due to overcharging and a higher internal cell temperature [52, 53]. Overcharging causes gas products to form from the oxidation of the electrolyte or of the sacrificial shut-down additives if they are present in the electrolyte. The ageing mechanisms described above arise at the cell level in various ageing modes: loss of lithium inventory (LLI), loss of active anode material (LAAM), loss of active cathode material (LACM), and rise in impedance [12]. The dominating mechanisms and modes of ageing depend on the charge-discharge protocol, environmental conditions, and cell design.

1.2.1 Effects of fast charging

Lithium-ion batteries should be capable of being rapidly charged in order to meet the expectations of the end-users. There is no standard and common definition for fast charging [54]. The charging rate defined in terms of C rate depends on e.g. the cell chemistry, cell design, and ambient conditions. The 1C rate is defined as the current the current required to fully discharge a battery that was at 100 % SOC in 1 hour.

Fast charging accelerates lithium plating and other side reactions [8, 10, 55, 56]. Under normal operating condition, lithium is intercalated between the graphite layers in stages. However, lithium plating can occur during charging when the rate of arrival of lithium on the graphite surface is faster than the intercalation, since lithium intercalation is a diffusion-limited process. Plating is accelerated at a high charge rate, low temperature, and high SOC where it is kinetically and thermodynamically favorable [55, 56]. The thicker graphite electrode used in energy-optimized cells increases the susceptibility to lithium plating because of the higher polarization and electrolyte transport limitation in the porous electrode [57, 58]. Plated lithium causes a capacity fade and a rise in impedance, and could potentially become a safety issue in extreme cases of dendrite formation and the

associated short-circuiting. Binder may decompose at a high charge rate possibly due to local heating or reaction with the plated lithium [59]. On the positive electrode side, fast charging has been linked to fragmentation and cracking of the secondary particles due to the DIS [60]. An increase in battery temperature associated with fast charging can also aggravate other side reactions that are dependent on temperature on both the positive and the negative electrode [10, 13, 61].

1.2.2 Effects of mechanical constraint

The compressive pressure in a lithium-ion battery can affect its performance and ageing [45, 46, 62-64]. External compressive pressure on a pouch cell increases the kinetic and mass transport resistance [63, 64], and it can also affect the ageing of the battery [45, 46, 62]. Arnold et al. reported that applying a small external pressure (~ 0.1 MPa) have a beneficial effect on battery lifetime [45]. External compressive pressure can reduce the capacity fading during high temperature excursion by reducing electrode layer delamination and electrolyte evaporation as reported by Zhao et al. [46]. It has been reported that prismatic cells age faster than cylindrical cells made from the same materials, and the difference has been attributed to the mechanically compact cell design of the latter [65].

1.2.3 Inhomogeneous ageing

The non-uniform distribution of temperature, current, and pressure that exists in a large-format cell or between cells in a battery module/pack can affect the battery performance and cause inhomogeneous ageing [48, 62, 66, 67]. Furthermore, the spatially different ageing rates on a lower length scale, for instance at the cell level, may interact with each other through uneven current distribution or heat generation developed between the cells and accelerate the overall ageing on a larger scale, at the module or pack level [44].

It has been reported that non-uniform conditions affect battery performance and ageing [41, 67, 68]. Troxler et al. reported that thermal gradient across a cell decreases the cell impedance compared to that of the average uniform temperature [67]. Klein et al. [41] reported that the current distribution between cells connected in parallel and individually kept at different temperatures is less uneven at a higher average temperature.

Fleckenstein et al. [68] modeled the effect of temperature gradient on battery ageing in the high energy prismatic cell (60 Ah) used in vehicle powertrains and reported that the thermal gradient did not cause additional acceleration of ageing. Offer et al. [69] compared the effects of surface cooling and tab cooling on the performance degradation of a 5 Ah pouch cell and reported that surface cooling caused higher useable capacity loss than the tab cooling when cycled at a higher C rate. The difference was attributed to the direction of thermal gradient being perpendicular to the layers of the pouch cell in the surface cooling case that led to inhomogeneous behavior and higher cell impedance, causing the voltage cut-offs reach earlier during operation and hence reduced usable capacity. With regard to pressure distribution, inhomogeneous lithium plating in cylindrical cells has been linked to a non-uniform compression in the cell leading to extensive plating at the characteristic locations following the pattern of the current tabs [62]. It has been claimed that the higher capacity fade under higher external compression is related to a non-uniform closure of separator pores leading locally inhomogeneous lithium plating and acceleration of the capacity fade [70].

2 Scope of the thesis

The aim of the work reported in this thesis has been to investigate the effects of charging rate and protocol, external compression, and inhomogeneities on lithium-ion battery ageing under fast charging conditions. The application in mind is electric vehicles, and both large-format cells and small single-layer pouch cells have been used. Large-format prismatic and cylindrical cells were used to investigate the ageing phenomena in a context relevant to electric vehicles. Small single-layer pouch cells were employed to understand the ageing and non-uniformities observed in the large-format cells in a controlled manner. NMC-based cells were used as their demand is increasing, especially by the automotive industry. The cell chemistry has a good combination of energy density, power density, thermal stability, and longer lifetime. Material characterization (SEM and EDS) and electrochemical techniques were used as tools for the investigation.

3 Experimental

Both commercial large-format cells (Papers I-II) and laboratory-scale single-layer pouch cells (Papers III-V) were used. The commercial cells can be directly relevant to electric vehicle applications, whereas the laboratory-scale cells are better for a more controlled testing. Electrochemical and material analyses techniques were used. Overviews of the materials, test set-up, ageing conditions, and analyses techniques are given here. Details can be found in the appended papers.

3.1 Materials

Three types of cells have been used.

Prismatic cell: A commercial 25 Ah energy optimized cell with a NMC (111) positive electrode and a graphite negative electrode was used. The dimensions of the cell were 148 x 26.5 x 91 mm (W x D x H).

Cylindrical cell: A commercial (INR 18650 Samsung SDI) 1.5 Ah power optimized cell with a NMC-LMO mixed positive electrode and a graphite negative electrode was used.

Single layer pouch cell: Laboratory-scale single-layer pouch cells constructed with NMC (111) and graphite electrodes were used. The electrodes were optimized for power (paper III) and energy (paper V) supplied by ElectrodesAndMore (USA). The separator used was a trilayer polypropylene/polyethylene/polypropylene Celgard 2320 with a thickness of 20 μm and a porosity of 39 %. The capacities of the cells used were either 10.17 mAh (paper III) or 13 mAh (paper V).

3.2 Test set-up

3.2.1 Pressure and temperature control

The pressure and temperature of the single-layer pouch cells were controlled by a rig developed in this work and shown in Fig. 3.1. The rig consists of a heat-resistant block made from polyether ether ketone (PEEK). High precision springs (Lesjöfors AB) were used to control the external compression on the sandwiched pouch cell by tightening it with nuts and bolts to a displacement of the spring corresponding to the required force. The force constant of the spring was 50 N/m. The temperature was

controlled by integration of a thermocouple, heating elements (Firedrod cartridge), and a feedback proportional-integral-derivative (PID) control system that heated the block when the battery surface temperature was below the set temperature and stopped heating when it was above the set temperature.

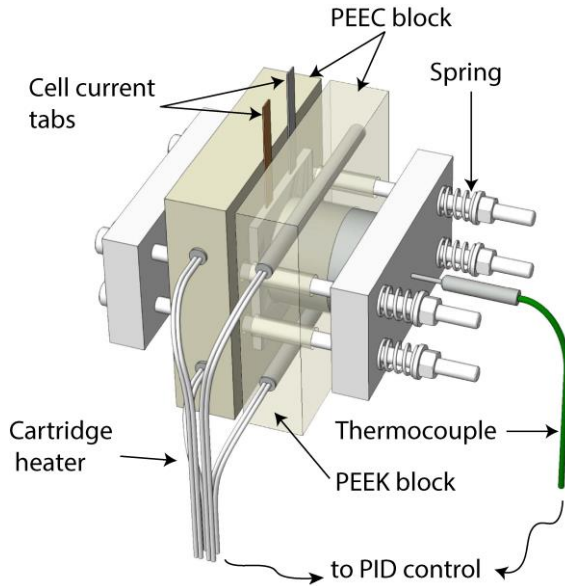


Fig. 3.1. Diagram of the cell temperature and pressure control rig.

3.2.2 Current distribution

The current distribution in a parallel cell configuration was measured by connecting a 5 mΩ shunt resistor (PRC 7, USA) in series with each member cell and measuring the voltage drop across the resistor with a differential multimeter (Keithley 2770, DMM). The current across each cell was then calculated from the quotient of the measured voltage drop and the resistance.

3.3 Ageing conditions

Prismatic cells (Paper I): Cells were cycled between 20 – 80 % SOC at charging rates of 1, 2, 3, and 4C corresponding to 25, 50, 75, 100 A, respectively. The corresponding upper and lower cut-off voltages for the given SOC range were based on the reference C/4 capacity value continuously updated after each reference test performed during the

cycling. In all cases, the discharging was done at 1C (25 A). The cells were kept in climate chambers set to 34 ± 1 °C during cycling.

Cylindrical cells (Paper II): Cells were cycled with three different charging protocols between 2.6 – 4.2 V, as shown in Fig. 3.2. In all cases, the discharging was performed at 1C with 5 minutes rest between each charging and discharging period.

Fast-partial charging: Cells were charged at 1.5C constant current.

CCCV-standard: Cells were charged at 0.5C constant current followed by a constant voltage charging at 4.2 V until the current dropped to 0.1 A.

CC-standard: Cells were charged at 0.5C constant current.

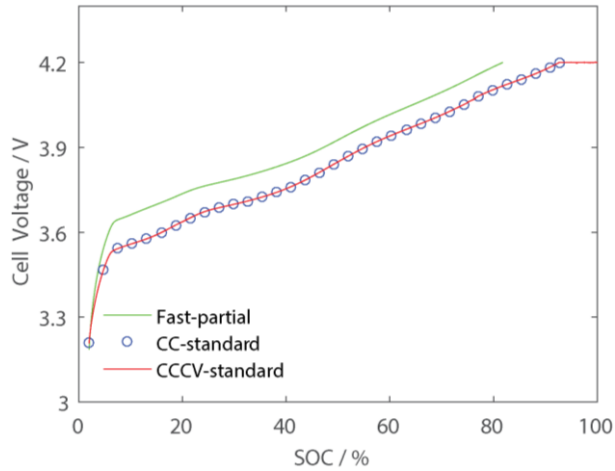


Fig. 3.2. Charging protocols used to cycle the cylindrical cells. [Note that the charging started at about 3.25 V after the previous discharge and rest time which are not shown here].

Single-layer pouch cells:

Pressure and pressure distribution study (Paper III): In order to investigate the effect of external compression on the ageing of single cells, four cells each subjected to 0.66, 0.99, 1.32, or 1.98 MPa external compression were cycled separately. In order to study the effects of the pressure distribution on ageing, two cells, one being subjected to 1.32 MPa and the other to 0.66 MPa compression, were connected in parallel and cycled. The result was compared with the cycling of a control group of parallel-connected cells, where both cells were subjected to 0.66 MPa compression. In all cases, cycling was performed between 3.445 – 4.1 V (25 – 85 % SOC based on C/25

cell capacity) at a 3C charge-discharge rate and at room temperature (24 - 28 °C).

Temperature and temperature distribution study (Paper V): Cells were cycled either between 3.445 – 4.1 V at a 1C charge-discharge rate or between 3.545 – 4.0 V at a 3C charge-discharge rate with 5-minute rest in all cases. The cells were cycled at 32, 36, 40 °C as single cells or connected in parallel with three cells at the given temperature levels and at the controlled compression pressure of 0.66 MPa.

3.4 Sample location

In order to investigate the spatially inhomogeneous ageing, samples were taken from different locations of the electrode jellyroll. Fig. 3.3 shows the locations investigated for the fast charging study (Paper I) (a) and for the curvature study (Paper IV) (b). Samples were designated as shown in Fig. 3.3a with reference to the location first along the jellyroll length and secondly along the jellyroll width. For example, a sample taken the half-way along the length and in the middle along the width is designated halfway-middle.

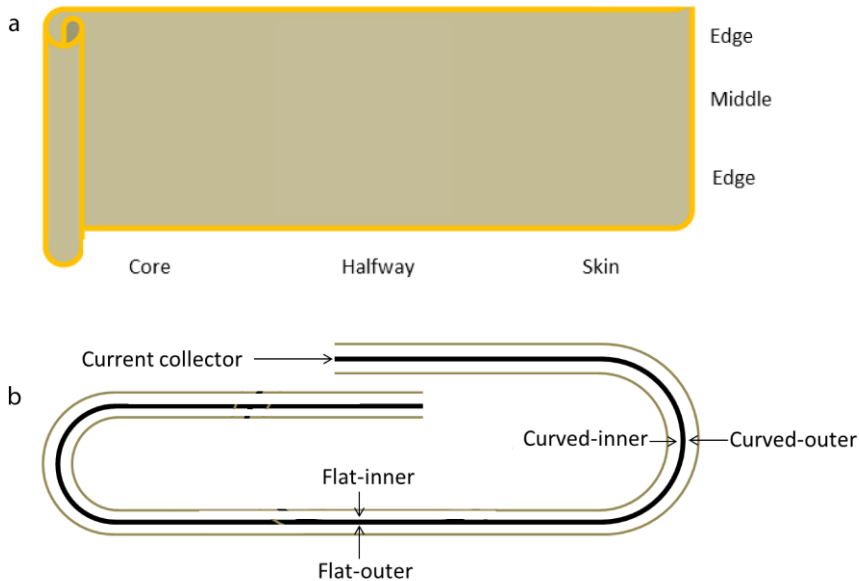


Fig. 3.3. Definition of sample locations for a prismatic cell jellyroll a) face view
b) edge view.

3.5 Analysis techniques

3.5.1 SEM and EDS

SEM images of the positive electrode, the negative electrode, and the separator were obtained in order to investigate the surface morphological changes induced by the ageing. A Carl Zeiss Sigma VP with accelerating voltage of 3 kV under vacuum (Paper I) or a Hitachi S-4800 field emission SEM (10 kV for the NMC/LMO electrode and 3 kV for the graphite electrode in paper II; 1 kV for the separator in paper III) equipped with an energy dispersive X-ray diffractometer (EDX) was used.

3.5.2 Electrochemical measurements

3.5.2.1 Capacity measurement

The capacity of full cells and half cells was measured at a low C-rate ($\leq C/20$, full discharging in 20 hours or more). Lithium foil was used as a counter electrode in the half cells (NMC/Li or Graphite/Li).

3.5.2.2 EIS measurement

Measurements were performed in symmetric cells of NMC/NMC and graphite/graphite constructed from electrodes obtained from half cells set to 3.95 V vs. Li/Li⁺ for NMC and to 120 mV (Paper I) or 0.86 V vs. Li/Li⁺ (paper II) for the graphite. In paper III, the electrodes for the symmetric cells were obtained directly from full cells set to a cell voltage of 3.665 V (50% SOC based on the C/25 cell capacity). EIS was measured in the frequency range of 100 kHz – 5 mHz by applying a 5 mV AC sinusoidal perturbation under open circuit condition.

3.5.3 Cell voltage fitting analysis

The ageing modes of a lithium-ion battery with regard to lithium inventory and active material losses can be diagnosed either with post-mortem experimental measurements or non-destructive online diagnostic techniques. The online diagnostic techniques have the advantage of minimizing the sampling bias in a large sample and avoiding the material disturbances which arise during post-mortem analysis, and they are also capable of tracking changes with time throughout the life of the battery. Their disadvantage is that they are limited in information. Different types of diagnostic techniques such as differential voltage analysis (dV/dQ, DVA),

incremental capacity analysis (dQ/dV , ICA), differential thermal voltammetry (dT/dV), and cell voltage fitting have been used by different authors [71-74]. In the present work presented in this thesis, the voltage fitting technique was used for a quantitative analysis of the ageing mode.

The voltage fitting was performed by opening a non-cycled cell, representative of the beginning of life (BOL) conditions, and building small half cells from it for each electrode to be used as input to the cell discharge curve fitting. The method of the fitting follows a similar principle described by Honkura et. al. [74, 75]. Fig. 3.4 shows the parameters of the fitting.

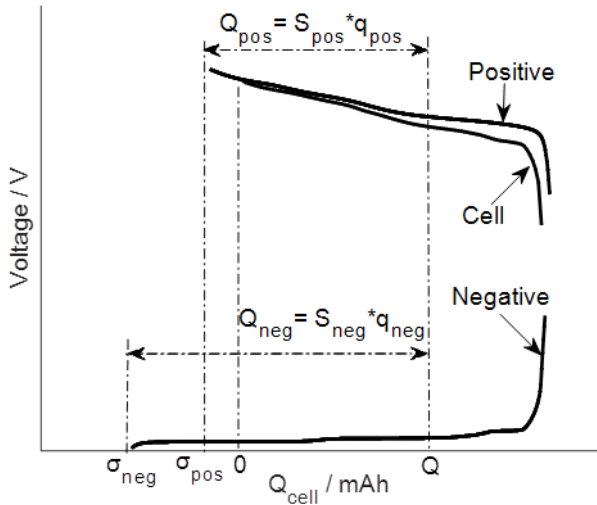


Fig. 3.4. Diagram of the cell discharge curve fitting technique.

The cell voltage is (V_{cell}) equal to the difference in the electrode potentials of the positive (V_{pos}) and the negative electrode (V_{neg}).

$$V_{cell}(Q) = V_{pos}(Q) - V_{neg}(Q) \quad (2.1)$$

where Q is the capacity of the cell discharged at a certain time t after the beginning of cell discharging between fully charged and fully discharged state.

When the cell is at Q , the potential of the positive electrode $V_{pos}(Q)$ is equal to its potential $V_{pos}(Q_{pos})$, when the electrode capacity is at Q_{pos} defined by the half-cell measurement. Since the electrode potential is independent of the size of the electrode, a small portion of the electrode (10 mm diameter

for instance) that can be characterized in separate half-cell measurement for capacity vs. voltage curve $v_{\text{pos}}(q_{\text{pos}})$ can be considered.

$$V_{\text{pos}}(Q) = V_{\text{pos}}(Q_{\text{pos}}) = v_{\text{pos}}(q_{\text{pos}}) \quad (2.2)$$

Similarly, for the negative electrode:

$$V_{\text{neg}}(Q) = V_{\text{neg}}(Q_{\text{neg}}) = v_{\text{neg}}(q_{\text{neg}}) \quad (2.3)$$

Substituting equations 2.2 and 2.3 in equation 2.1 gives

$$V_{\text{cell}}(Q) = v_{\text{pos}}(q_{\text{pos}}) - v_{\text{neg}}(q_{\text{neg}}) \quad (2.4)$$

Q can be defined in terms of the scaling factor S_{pos} (where S_{pos} is the ratio of the mass of the active positive electrode material in the cell jellyroll to that of the 10 mm diameter positive electrode taken for the analysis) and the positive electrode shift δ_{pos} (unused capacity of the positive electrode before the start of the cell discharge):

$$Q = Q_{\text{pos}} + \delta_{\text{pos}} = S_{\text{pos}} * q_{\text{pos}} + \delta_{\text{pos}} \quad (2.5)$$

So that:

$$q_{\text{pos}} = \frac{Q - \delta_{\text{pos}}}{S_{\text{pos}}} \quad (2.6)$$

Similarly, for the negative electrode

$$q_{\text{neg}} = \frac{Q - \delta_{\text{neg}}}{S_{\text{neg}}} \quad (2.7)$$

Substituting equations 2.6 and 2.7 in equation 2.4 gives for the fitting:

$$V_{\text{cell}}(Q) = v_{\text{pos}}\left(\frac{Q - \delta_{\text{pos}}}{S_{\text{pos}}}\right) - v_{\text{neg}}\left(\frac{Q - \delta_{\text{neg}}}{S_{\text{neg}}}\right) \quad (2.8)$$

Equation 2.8 is fitted the experimental cell voltage curve using half-cell measurements. The fitting provides optimized values of the shifts (δ_{pos} , δ_{neg}) and scaling factors (S_{pos} and S_{neg}), and these parameters are used to track changes with ageing.

The decrease in the active material of the positive electrode (Loss of active cathode material, LACM) is calculated by taking the ratio of the scaling factor at the EOL ($S_{\text{pos,EOL}}$) to that at the BOL ($S_{\text{pos,BOL}}$).

$$\text{LACM}(\%) = 100 * \left(\frac{S_{\text{pos,EOL}}}{S_{\text{pos,BOL}}} \right) \quad (2.9)$$

The loss of the negative electrode active material (Loss of Active Anode Material, LAAM) is obtained in an analogous manner

$$\text{LAAM}(\%) = 100 * \left(\frac{S_{\text{neg,EOL}}}{S_{\text{neg,BOL}}} \right) \quad (2.10)$$

The loss of lithium inventory (LLI) due to cycling is estimated by the integral of the difference in the amount of lithium that leaves the negative electrode but does not enter the positive electrode during the cell discharge. The rate of lithium that leaves the negative electrode is $S_{\text{neg}} * dq_{\text{neg}}/dt$ and that enters the positive electrode is $S_{\text{pos}} * dq_{\text{pos}}/dt$, and the difference is:

$$\frac{d}{dt}(\text{LLI}) = S_{\text{neg}} * \frac{d}{dt}(q_{\text{neg}}) - S_{\text{pos}} * \frac{d}{dt}(q_{\text{pos}}) \quad (2.11)$$

Which leads to:

$$\frac{d}{dt}(\text{LLI}) = \frac{d}{dt}(\delta_{\text{neg}} - \delta_{\text{pos}}) - q_{\text{neg}} * \frac{dS_{\text{neg}}}{dt} + q_{\text{pos}} * \frac{dS_{\text{pos}}}{dt} \quad (2.12)$$

Integrating equation 2.12 gives the loss of lithium inventory in the time interval between t_1 and t_2 , where the reference performance tests were performed.

$$\Delta \text{LLI} = \left(\delta_{\text{neg}}(t_2) - \delta_{\text{pos}}(t_2) \right) - \left(\delta_{\text{neg}}(t_1) - \delta_{\text{pos}}(t_1) \right) - \langle q_{\text{neg}} \rangle * (S_{\text{neg}}(t_2) - S_{\text{neg}}(t_1)) + \langle q_{\text{pos}} \rangle * (S_{\text{pos}}(t_2) - S_{\text{pos}}(t_1)) \quad (2.13)$$

where $\langle q_{\text{neg}} \rangle$ and $\langle q_{\text{pos}} \rangle$ are the average values of the electrode capacities in an area with 10 mm diameter in the cycled cell between time t_1 and t_2 . Usually, all the terms on the right-hand side of equation 2.12 are negligible

except for the first term. The loss of lithium inventory between times t_1 and t_2 can thus be approximated by:

$$\Delta LLI \approx \delta_{\text{neg}}(t_2) - \delta_{\text{pos}}(t_2) - \delta_{\text{neg}}(t_1) + \delta_{\text{pos}}(t_1) \quad (2.14)$$

The total LLI from any time t_i to a given time t_j is calculated as the summation of ΔLLI between the two times.

$$LLI = \sum_{t_i}^{t_j} \Delta LLI \quad (2.15)$$

4 Results and discussion

This section summarizes the main results of the papers appended to the thesis. It is divided into three parts: effects of charging rate, of compression pressure, and of inhomogeneity on lithium-ion battery ageing. The effects of inhomogeneity include those caused by curvature in the prismatic cell and by uneven current distribution in the parallel-connected single-layer pouch cells. The uneven current distribution covers that caused by uneven distribution of temperature and of external compression pressure.

4.1 Effects of charging rate on ageing

4.1.1 Capacity fade

The capacity fade as a function of equivalent full cycle is shown in Fig. 4.1a for the prismatic cells cycled at 1C – 4C charging rates. It can be seen that capacity fade increased with increasing charging rate except at 2C which showed a slower fading than the 1C. The slower ageing in the case of 2C charging is associated with its shorter calendar time at a certain equivalent cycle during cycling compared to the 1C. When the capacity fade is plotted as a function of time in Fig. 4.1b, the 1C charging shows a slower capacity fade.

Three distinct stages of capacity fading, also reported previously [76-78], can be observed in Fig. 4.1. Stage 1 includes a high rate capacity fading from the beginning of cycling for a certain number of cycles followed by a decelerating capacity fade in stage 2. In stage 3, the cells show an acceleration of the capacity fading. Cells cycled at 1C - 3C show stage 1 that can be explained by a fast lithium-ion loss to surface film formation (ex. SEI). As the film grows thicker, its passivating property decreases the rate of lithium ion loss in stage 2. The cell cycled at 3C charging rate additionally shows stage 3, which has been suggested to be a sign of lithium plating or a change of the limiting electrode from the anode to the cathode during cell discharge [62, 76, 77]. Significant lithium plating was observed in this work in the cell cycled at 3C. The cell cycled at a 4C charging rate showed a distinct behavior – stage 1 for a short number of cycles after which it jumped directly to stage 3, and eventually to sudden death after about 300

full equivalent cycles. The sudden death was due to activation of the current interrupt device (CID) which irreversibly disconnected the positive tab from the jellyroll. The CID is activated by a high internal cell pressure as a result of excessive gas evolution. The excessive gas evolution and high internal pressure are indicated by the large swelling of this cell from a thickness of 27 ± 1.5 mm at the BOL to 40 mm at the EOL, compared with ~ 32 mm for the other cells.

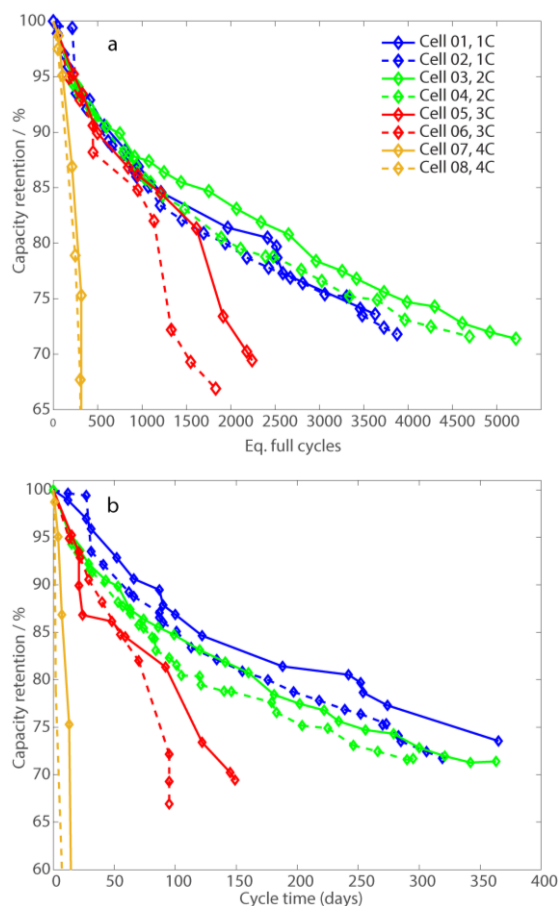


Fig. 4.1. Normalized C/4 capacity fade of the prismatic NMC/graphite cell cycled between 20 and 80% SOC at 34 ± 1 °C as a function of a) equivalent full cycles (50 Ah capacity throughput) b) time (days).

4.1.2 Comparison of fast charging and full charging

It is common to carry out fast charging only to a partial state of charge ($\sim 80\%$ SOC) at public charging stations, since charging the last $\sim 20\%$ to full capacity (100% SOC) takes a disproportionately longer time because of the significant reduction in charging current beyond $\sim 80\%$ SOC. In contrast, charging at home overnight is performed at a slow rate and commonly to 100% SOC. It is interesting to compare these two charging methods to see which factor, higher SOC or higher charging current, has the greatest effect on the ageing. Fig. 4.2 shows the capacity fade of the 18650 cylindrical cell (1.5 Ah) cycled according to the different charging protocols shown in Fig. 3.2. It can be seen that fast charging to a partial SOC level shows the least rate of capacity fade while the slow charging to 100% SOC shows the fastest rate. The cell charged at 0.5C constant current (CC standard) has an intermediate ageing rate. This indicates that full charging was in this case more detrimental to the battery life than the fast charging. This result is supported by Tanim et al. [44] who compared the ageing of single cells at $\sim 2\text{C}$ fast charging with the ageing at a slow charging at $\sim 0.14\text{C}$, charged to 100% SOC in both cases, and reported that the fast charging had similar capacity fading to the slow charging.

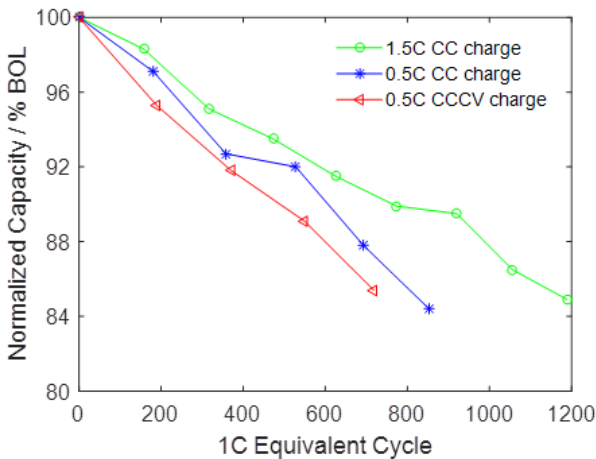


Fig. 4.2 Capacity fading of 18650 cylindrical cells cycled according to the three different charging protocols shown in Fig. 3.2.

In order to investigate the reason for the faster ageing in the cases of slower charging (0.5C CC charge and 0.5C CCCV charge), calendar ageing of cells at 50% and 100% SOC was performed (Supplementary information in Paper II). The results show capacity fade with calendar ageing was negligible compared to that due to the cycle ageing. The observed trend could not therefore be due to the calendar time. Another difference between the cells during cycling was the cell temperature due to self-heating. Even though the cells were cycled in a climate chamber set at 25 °C, the cell temperature was different from that of the surrounding environment. The maximum temperature measured on the cell surface during cycling at 0.5C and 1.5C were 26.5 and 30 °C, respectively. It may be claimed that the higher cell temperature during the fast charging facilitates lithium intercalation and deintercalation, but the EIS performed at 26.5 and 30 °C showed only 4% difference in impedance at 10 mHz frequency (123 mΩ at 26.5 °C and 118 mΩ at 30 °C). The higher temperature also facilitates side-reactions other than lithium intercalation and deintercalation. Hence, the temperature could not be the reason for the observed trend in ageing, and only the state of charge range (Δ SOC) was thus probably be the main reason. This claim is supported by the non-linear accelerated ageing above 90% SOC reported for NMC cells by Bendikt et al. [79].

From the results of the prismatic cell and cylindrical cell studies, it appears that the ageing of commercial NMC cells is less sensitive to fast charging up to a certain C rate, for instance 2C in the tested cases. Instead, other factors such as the SOC range determine the rate of ageing. This applies only to single cells. In EVs that use multiple cells in a battery pack, thermal issues can arise and fast charging at about 2C may show faster ageing than a slower charging. For instance, Tanim et al. [44] reported a significant difference in capacity fade between 2C and 0.14C charging when a pack was tested but not when the test involved only a single cell. They attributed this difference to thermal issues in the battery pack due to self-heating at the high charging rate.

4.1.3 The dominant capacity fading mode

A voltage-fitting analysis was carried out in order to quantify the ageing modes non-destructively in terms of LLI, LACM, and LAAM. Fig 4.3 (a-b) shows the results for the prismatic and cylindrical cells, respectively. The cell capacity loss and the LLI were similar in the two cases, indicating that

the LLI is the dominating mode of ageing which determines the cell capacity loss. Although there is some loss of active material, this does not affect the cell capacity loss because excess material is present at the end of charging or discharging at both the BOL and EOL of the cycled cells. In addition, LACM is higher than LAAM, which indicates that the positive electrode is important for the loss of active electrode material.

In Fig 4.3a, there is a significant difference in active material loss between that calculated from the voltage fitting and that experimentally derived from the post-mortem analysis. The discrepancy in the NMC electrode could be due to the fact that the samples analyzed were not fully representative of the entire cell. For instance, if there was a partial loss of contact between the active electrode layer and the current collector, this would not be evident in the experimental measurement. When the prismatic cells were opened, considerable layer delamination was observed, but the samples were taken only from locations where there was no significant active layer delamination, and an external clamping load was applied during the capacity measurement. These two factors could cause the experimentally measured capacity loss to be lower than the calculated values, leading to the discrepancy evident in Fig. 4.3a. The calculated value should be more representative of the average of what is actually happening in the cell, since it includes material losses not observed in the post-mortem analysis. In case of the graphite, it was brittle and fragile and some of the material may thus have been lost during the electrode cutting to make the half-cells for the capacity measurement. The measured capacity loss in graphite may thus be slightly higher than the calculated value. The discrepancy in the LACM observed in the prismatic cell was much lower in the case of the cylindrical cell as shown in Fig. 4.3b. This could be due to the more compact design of the cylindrical cell or to a manufacturing quality difference between the two types of cell. When the cylindrical cell was opened, the positive and negative electrode jellyrolls were relatively intact. The above results demonstrate the significance of the non-destructive technique in determining the internal state of battery health to complement a post-mortem analysis.

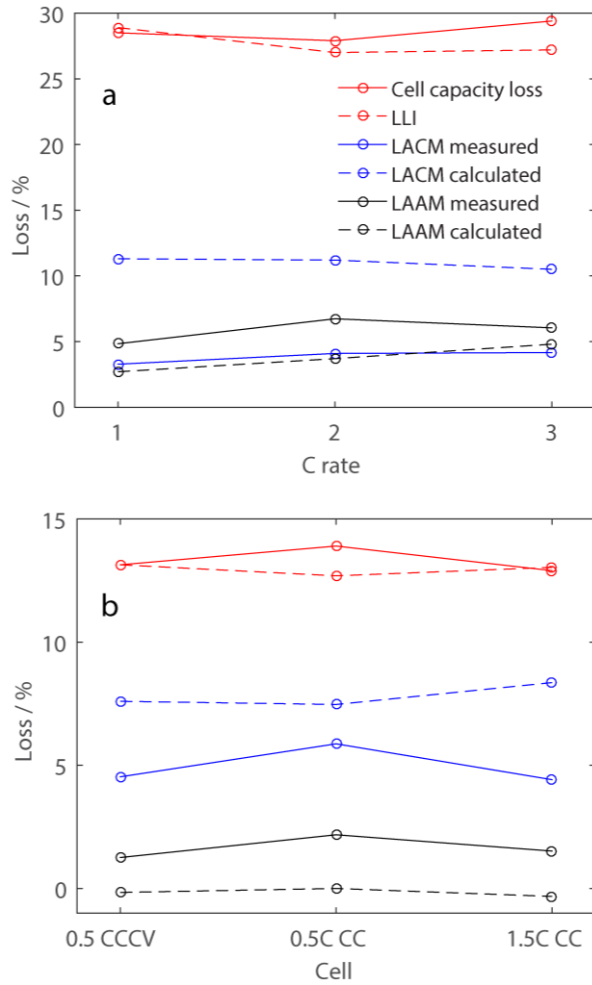


Fig. 4.3. Capacity fading modes of a) the prismatic and b) the cylindrical cell.

4.1.4 Impedance rise

Fig. 4.4 shows the 2 ms direct current internal resistance (DCIR) as a function of equivalent cycle number for pairs of cycled prismatic cells. The order of impedance rise follows the same order as that of the capacity fade (Fig. 4.1) viz. $2C < 1C < 3C < 4C$.

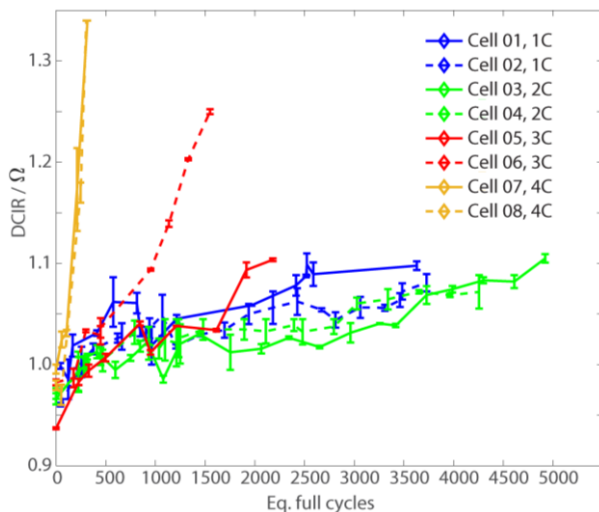


Fig. 4.4. 2 ms direct current internal resistance as a function cycle number for pairs of prismatic cells that were cycled at a charge rate of 1C – 4C.

The impedance of electrodes was measured in a symmetric cell set-up in order to investigate the contribution of the electrodes to the total rise in cell impedance. Fig. 4.5 (a-b) shows the impedance change of the NMC/NMC and graphite/graphite symmetric cells, respectively, taken from the prismatic cell. The impedance of both electrodes increased with cycling, contributing to the rise in cell impedance. The notable change in the NMC electrode impedance was in the diameter of the high frequency semi-circle in the frequency range from 100 KHz to 2 Hz. The impedance in this range is usually attributed to surface film resistance to ionic migration, to contact resistance between the current collector and the active electrode layer, and to contact resistance among electrode particles themselves or with the carbon conductive additive. The width of the semi-circle and the diffusion length in the Nyquist plot for the graphite electrode in Fig 4.5b increases with cycling, indicating an increase in both the charge transfer and diffusion resistance. Both the NMC and the graphite electrodes taken from the 4C cell show lower increase in impedance than the electrodes taken from the other cells cycled at charging rates of 1C-3C. This is in contrast to the order of the cell impedance rise, where the cell cycled at a charging rate of 4C showed the greatest rise in impedance. This could be due to some factors that

cannot be identified in the post-mortem analysis on the electrodes such as ionic transport restriction due to gas bubbles trapped between the electrodes in the jellyroll or even to electrolyte evaporation induced by the higher joule heating in the cell.

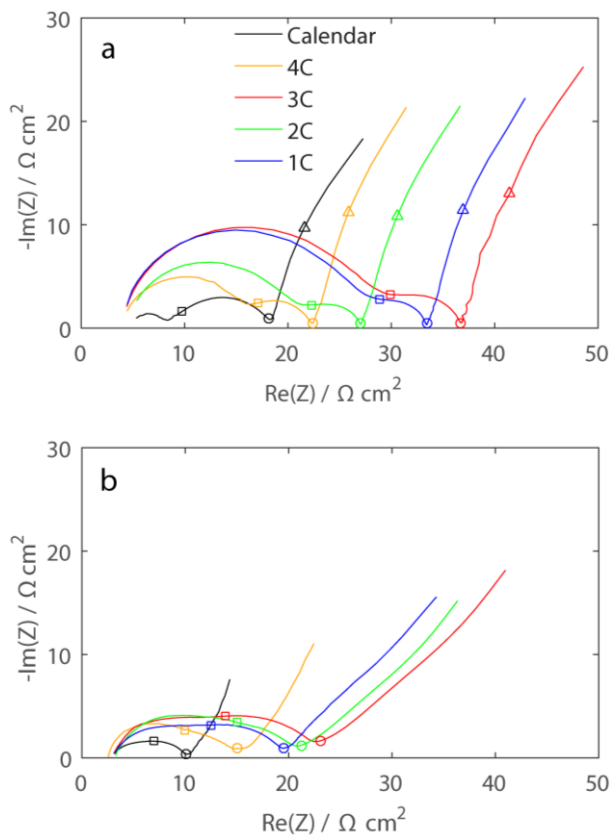


Fig. 4.5. Nyquist plots of a) NMC/NMC and b) graphite/graphite symmetric cells taken from the prismatic cells that were cycled at charging rates of 1C, 2C, 3C, and 4C between 20 and 80 % SOC at 34 ± 1 °C.

Fig. 4.6 (a-b) shows the electrochemical impedance of the positive (NMC/LMO) and negative (Graphite) electrodes taken from the cylindrical cells. The total increase in impedance at EOL (~ 15 % capacity loss) is similar in the two electrodes irrespective of the charging protocol, indicating that the ageing mechanism is possibly independent of the path to

the EOL. Furthermore, the change in the high-frequency semi-circle for the NMC/LMO electrode taken from the cylindrical cell after cycling (Fig. 3.6a) was much lower than that of the NMC electrode taken from the prismatic cell (3.5a). Since the impedance in this region is strongly related to the contact between the current collector and the active electrode, this may imply that the cylindrical cells have a good performance in limiting the contact loss due to its compact geometry.

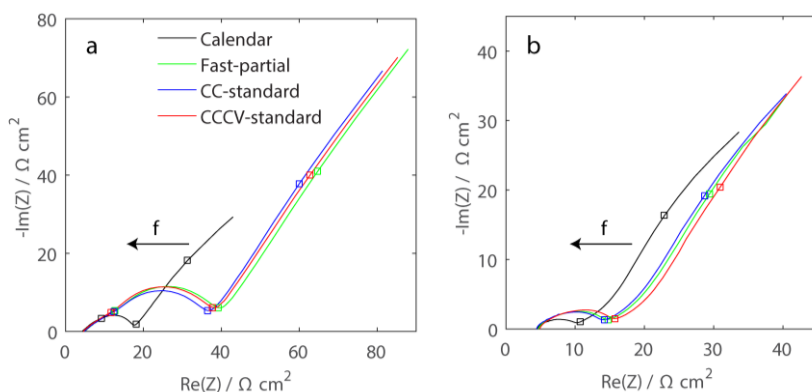


Fig. 4.6. Nyquist plots of a) the positive and b) the negative electrode symmetric cells taken from the cylindrical cells cycled according to the three different protocols shown in Fig. 3.2. [a] \square represents 50 Hz, 1 Hz and 10 mHz. b) \square represents 1 Hz and 10 mHz.].

4.1.5 Main ageing mechanisms

Fig. 4.1 shows that a charging rate higher than 2C significantly shortens the battery life, below the acceptable cycle life of 4000 or more cycles. In order to help push the limits of charging capability beyond 2C, while achieving the minimum cycle life requirement, it is necessary to identify the ageing mechanism that leads to premature failure of the battery.

Extensive gas evolution and subsequent activation of the CID leading to the irreversible rupture of the positive tab from the jellyroll was observed with the aggressive charging rate of 4C. The rupture caused the cell to die and no further charging and discharging of the cell was then possible. Gas evolution can originate from either the positive or the negative electrode. Overcharging the cell can produce gas due to oxidation of the electrolyte

and the shut-down additives if present in the electrolyte. The results of the cell voltage fitting analysis and of the post-mortem analysis of the electrodes showed however that gas evolution from the positive electrode probably did not occur in our case. A cyclic voltammetry test performed NMC/Li half-cell using the electrolyte taken from an opened cell showed an oxidation peak at ~ 4.5 V vs. Li/Li⁺. During the cycling, the cell voltage was never allowed to be above 4.15 V and cell voltage fitting showed that the positive electrode potential was limited to below 4.2 V vs. Li/Li⁺. Local hotspots and inhomogeneities are expected, but overpotentials of more than ~ 0.3 V that can initiate the oxidation are not expected. Gas evolution has been linked to a fast cyclable lithium loss and active material loss (graphite exfoliation) in literature [10] which were both seen in the cell cycled at 4C. The 4C cell lost 21% of the C/4 capacity in less than 300 equivalent full cycles compared to about 27% for the other cells cycled with charging rates of 1C, 2C, and 3C in about 4750, 3750, and 2000 equivalent full cycles, respectively. Graphite exfoliation can be seen from the SEM micrograph in Fig. 4.7d. The corresponding graphite active material loss has also been seen (Paper I, Fig. 7d). The loss of accelerated cyclable lithium loss and of graphite active material (graphite exfoliation) points to the graphite electrode as the source of the gas evolution. However, no further study was conducted to confirm this.

Extensive lithium plating was observed in the cell cycled at a charging rate of 3C, as shown in Fig. 4.7c. The lithium plating was observed visually showing gold like deposits on the unwound jellyroll. The fact that extensive lithium plating was observed at a charging rate 3C but not at 4C is interesting and may indicate that lithium plating has occurred later during battery cycling. Fig. 4.5b shows that the graphite taken from the 3C cell had much larger impedance than that taken from the 4C cell after the long-term cycling. If the impedance of the graphite is larger, it is expected to be more susceptible to lithium plating, especially during fast charging.

Fast-charging is also expected to accelerate the particle cracking of positive electrode due to the diffusion-induced stress. In our case, however, particle cracking was observed even at the lower charging rates of 1C and 2C in cells that were cycled for the acceptable number of cycles (Fig. 4.7f) but not in the cell charged at 4C (Fig. 4.7h). Cracking was also observed after both the

slow charging at 0.5C and the fast charging at 1.5C in another publication [80]. This indicates that particle cracking is not dependent on fast charging rate but can even occur during slower charging.

It appears that cyclable lithium loss, gas evolution, and lithium plating are the main ageing mechanisms that limit fast charging in terms of battery life. In order to push the limits of charging to higher charging rates, consideration must primarily be given to these mechanisms that limit the cycling performance.

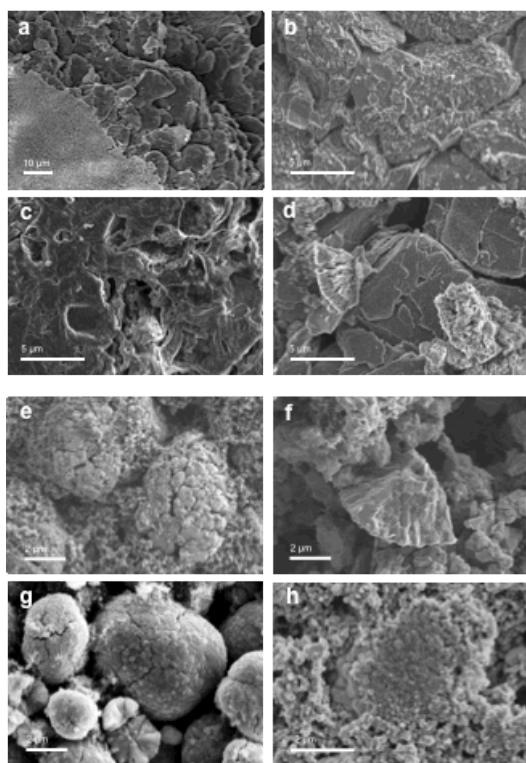


Fig. 4.7 SEM images of (a-d) negative electrodes and (e-g) positive electrodes. a) Calendar-aged (cal) showing the Al_2O_3 coating; b) surface structure found on cal, 1C and 2C (picture taken from 1C); c) Li-plated surface structure on 3C; d) Exfoliation on 4C; e) Typical particle agglomerates on cal, 1 and 2C (picture taken from 1C); f) cracked particles found on 1 and 2C (picture taken from 1C); g) "naked" particles on 3C and h) covered particle without cracks on cal. and 4C (picture taken from 4C).

Overall, the capacity and impedance of both the NMC-based positive electrode and the graphite negative electrode are affected by the cycling. This is different from the LFP-based commercial cells where only the graphite electrode was usually reported to be significantly affected by cycling [48, 81-83]. This shows that shifting from LFP to NMC-based lithium ion commercial batteries shifts the focus of ageing from only graphite to both the positive and the negative electrodes.

4.2 Effects of compressive pressure on ageing

The electrode jellyrolls in the different cell formats are subjected to compression pressure from the cell casing, from an externally applied compression, or from the dead weight of stack of cells. This pressure can increase as the cell swells due to electrode swelling, SEI growth, and/or gas evolution inside the cell. Such pressure on the jellyroll may affect the performance and ageing of batteries and requires further investigation.

4.2.1 Initial performance

The cell impedance is shown as a function of external compression pressure in Fig. 4.8. Fig. 4.8a shows that the impedance of the full cell increases with increasing applied pressure. The change in diameter of the semi-circle and in length of the Warburg tail indicates that the external compression affects the kinetics and mass transport properties of the cell. This can be due to a decrease in porosity and to a lowered contact between the electrolyte and the electrode particles under a high pressure. The semi-circle width changed almost linearly with increasing pressure, as shown in the inset of Fig. 4.8a. Impedance tests performed on symmetric NMC/NMC and graphite/graphite cells (Fig. 8 b-c) indicated that both the NMC and the graphite electrode contribute to the change in impedance with pressure, but that only graphite contributes to the change at the Warburg tail of the full cell. In Fig. 4.8, the impedance where the imaginary part of the impedance crosses the real axis, referred to as the high frequency resistance (HFR), does not change with pressure, except for a slight change at 1.98 MPa. This indicates that the pressures applied were all sufficient to make good contact between the different battery components. At these pressure levels, EIS on a cell consisting of an electrolyte-soaked separator sandwiched between two planar copper foils showed that the increase in the HFR at 1.98 MPa was due to the separator. The HFR in the separator cell changed only slightly under a pressure of 1.98 MPa (Paper III).

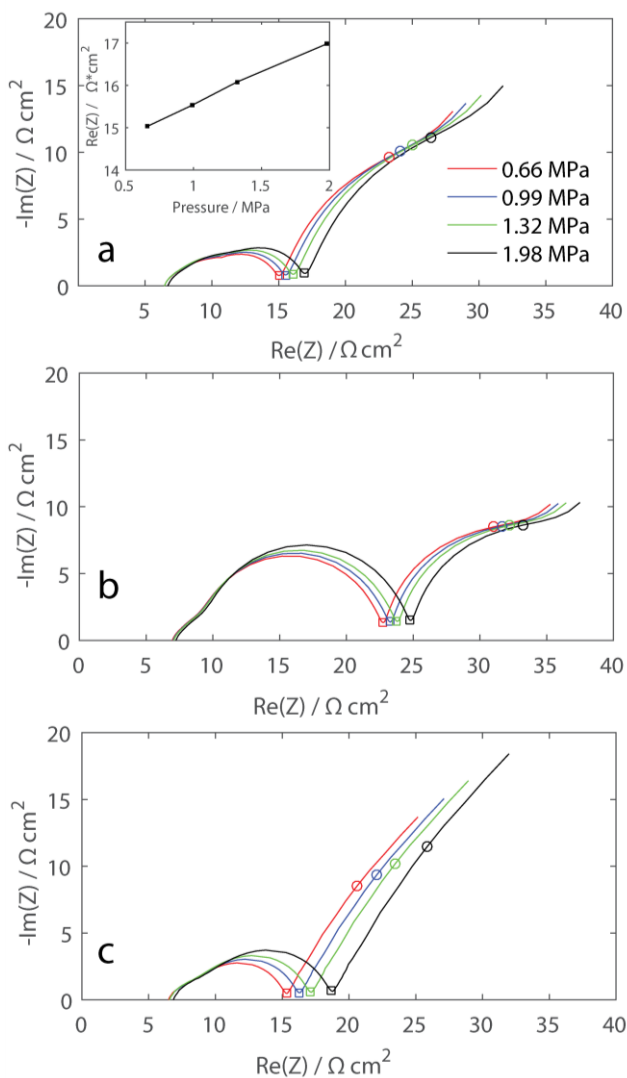


Fig. 4.8 Impedance as a function of pressure for a) a full cell (inset: impedance at 10 mHz frequency as a function of pressure.) b) a NMC/NMC symmetric cell c) a graphite/graphite symmetric cell. [The full cell was at 50% SOC (3.665 V), the electrodes in b-c were taken from two duplicate full cells at 50 % SOC].

4.2.2 Cycling

4.2.2.1 Capacity loss

Fig. 4.9a shows the change of the normalized discharge capacity with cycling. The highest (1.98 MPa) and the lowest (0.66 MPa) applied pressures increased the rate of capacity loss, whereas the medium pressure levels, especially 1.32 MPa, were beneficial in reducing the rate of capacity loss. Since the 3C discharge capacity measured during cycling is highly influenced by cell impedance, the low rate (C/25) capacities of the cycled cells were measured at the EOL and the results are shown in Fig. 4.9b. It shows that the cell cycled under 1.32 MPa compression retained the maximum capacity at the EOL compared with the other cells.

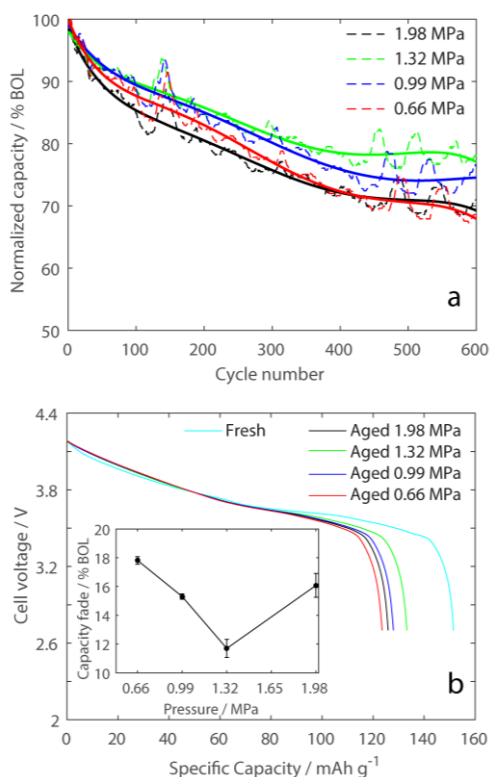


Fig. 4.9 a) Normalized 3C discharge capacity as a function of cycle number for cells subjected to cycle ageing under compression pressures of 0.66, 0.99, 1.32, and 1.98 MPa. b) C/25 discharge capacity of a fresh cell and of the cycled cells aged under 0.66, 0.99, 1.32 MPa, 1.98 MPa at the EOL.

Fig. 4.10 shows the capacity of (a) NMC and (b) graphite electrodes taken from a fresh and the cycled cells. The capacities of the NMC and graphite electrodes cycled under various pressure levels are similar at the EOL, regardless of the pressure applied during the cycling, showing that the difference in capacity loss is due not to a difference in the loss of active materials from the positive and negative electrodes. On the other way, this indicates that the difference was rather due to the cyclable lithium loss. It can thus be concluded that the optimum pressure is beneficial to the battery life by reducing the loss of the cyclable lithium. The fact that the optimum pressure reduces the loss of cyclable lithium and not the loss of active material is an indication of a coupling between the electrochemistry and the mechanics.

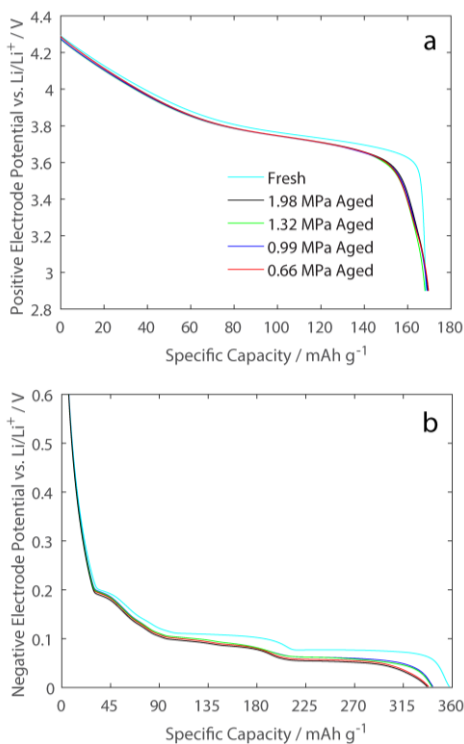


Fig. 4.10 Specific capacities of electrodes taken from the fresh and cycled cells of a) NMC b) Graphite.

One important implication of the existence of an optimum pressure that extends battery life is that it can explain some of the discrepancies in the ageing trends reported by different authors [48, 62, 66]. Some authors have reported an increasing ageing while others a decreasing ageing towards the core along the jellyroll length of a cylindrical cell. If the pressure levels in the cell were less than the optimum, a decreasing ageing could be observed towards the core, but if the pressure levels in the cell were higher than the optimum, an increasing ageing could be observed.

4.2.2.2 Mechanism of capacity loss

During battery cycling, a loss of cyclable lithium has been associated with a cracking of the SEI layer as the volume of the graphite particles changes during lithiation and delithiation, continuously exposing new graphite surfaces for contact with the electrolyte and the growth of SEI as a result. Several techniques such as aluminium coating that limit SEI cracking has been suggested to stabilize the SEI layer [84-88], and an externally applied compression may have the same effect as well. This hypothesis is supported by the fact that the optimum pressure extends the cycle life by reducing loss of cyclable lithium which is the main effect of SEI growth. Nevertheless, a pressure higher than the optimum decreases the battery life. This can be due to the retarded electrochemical reaction and mass transport at the highest applied pressure, which facilitates side-reactions instead of the normal lithium intercalation and deintercalation in the graphite. On the other hand, Arnold et al. [45] have claimed that the greater loss of capacity at the higher pressure is due to locally non-uniform closure of the separator pores, which accelerates lithium plating due to the high overvoltage close to the closed pores. In our case, non-uniform pore closure has been observed, as shown in Fig. 4.11(a-d). In order to see whether the non-uniform pore closure is the cause of or the result of the ageing, the HFR of separators taken from the aged cells was measured. The HFR in Fig. 4.10f more or less follows the capacity loss, indicating that the pore closure was the result of the capacity loss and not the reason for it. If the pore closure were the reason, the HFR would directly increase with increasing pressure.

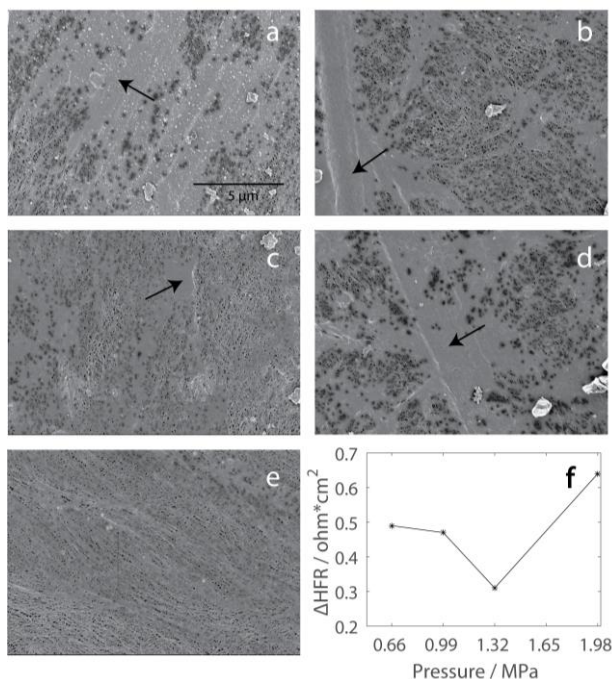


Fig. 4.11. SEM images of separators taken from cells cycled under pressure of: a) 0.66 MPa b) 0.99 MPa c) 1.32 MPa d) 1.98 MPa. e) SEM image of separator taken from a fresh cell. f) Increase in the HFR of separators from the cycled cells with respect to the HFR of a fresh separator.

4.3 Inhomogeneous ageing

Usage of a large-format cell and their interconnection involves the effects of inhomogeneous distribution of mechanical constraint, temperature, and current. This inhomogeneity may lead to non-uniform ageing in the large-format cell or in the group of connected cells. Non-uniform ageing along the length and width directions of a prismatic cell jellyroll has been observed after cycling the prismatic cells and the result is shown in Fig. 4.12. More ageing is seen going from the cell skin towards the core of the jellyroll. Such differences could be due to spatial differences in temperature and pressure during cycling. The following sections present the results of non-uniform ageing caused by jellyroll curvature in a prismatic cell and by current distribution. The current distributions are in these cases caused by temperature distribution and pressure distribution.

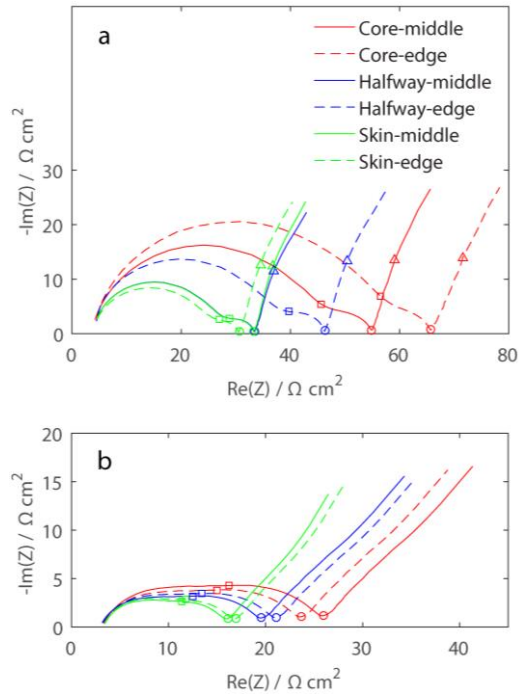


Fig. 4.12 Nyquist plots showing impedance of symmetric cells for locations defined in Fig. 2.1 a) NMC/NMC b) Graphite/graphite. [Samples for the test were taken from the prismatic cell cycled at 1C charging rate].

4.3.1 Effects of jellyroll curvature

Mechanical constraints can originate from the geometry of the cell. For instance, the bending of the jellyroll following the curvature of a prismatic cell casing induces a bending stress which does not exist in the flat regions. Fig. 4.13 shows the impedances of samples taken from different locations of the prismatic cell (Fig. 3.3) that was cycled for about 4000 cycles at a 1C charge-discharge rate between 20 and 80 % SOC. It can be seen that the impedance at the outer radius of curvature in the curved region is significantly greater than that of samples from the internal radius of curvature and from the flat regions. The most notable difference was observed in the semi-circle at high frequency. In the literature, the impedance in this frequency range has been attributed to the resistance of the surface film to ion migration and to the contact resistance between the current collector and the active electrode layer or within the active layer, between active particle to active particle or active particle to conductive

additive [89-93]. The difference decreases from the cell core (Fig. 4.13a) towards the skin (Fig. 4.13b) with a larger radius of curvature along the jellyroll length, indicating that the curvature effect is pronounced at the core.

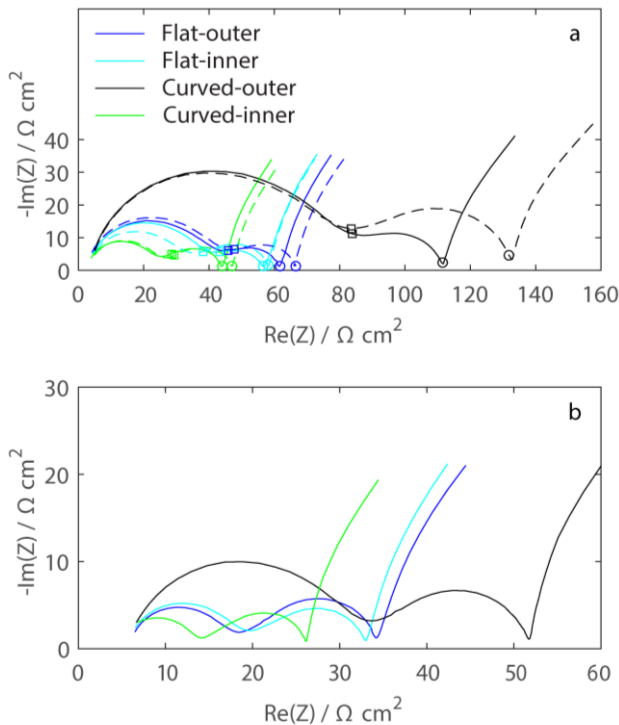


Fig 4.13. Nyquist plots of NMC/NMC symmetric cells taken from a) the core (radius of curvature = 9 mm) and b) towards the cell skin (radius of curvature = 12 mm) of the prismatic cell jellyroll.

In order to investigate the reason for the impedance rise at the high frequency semi-circle and the variation of the impedance depending on the location, impedance measurements were made under various compression loads and at different temperatures in the case of the curvature samples taken from towards the cell skin (Fig. 4.13b). Varying the compression load and temperature makes it possible to see whether there is a contact loss at any of the material interfaces. It is expected that a contact between different materials will change with compression load but that it will be less sensitive

to temperature variations. Fig. 4.14 (a and b) show the impedance under different compression loads and temperatures, respectively. It can be seen in Fig. 4.14a that the diameter of the semi-circle at the high frequency ($2h_1$) changed significantly with compression, especially for the sample at the outer radius of curvature, indicating that it is the contact loss that causes the sample to have the largest impedance. Fig 4.14b shows that $2h_1$ changes little with temperature compared to the change with changing compression load, supporting the conclusion that the high impedance of the sample at the outer radius of curvature is primarily due to contact loss. However, $2h_1$ increase to some extent with decreasing temperature in Fig. 4.14b, indicating that the impedance in the high frequency semi-circle has some contribution from other sources, such as ionic migration resistance through the electrode surface film [89], although it is dominated by the contact resistance.

The contact loss can occur at different material interfaces between: the current collector and active layer, active particle and carbon additive, and active particle and active particle contacts. Measuring the electronic conductivity of the active layer on samples taken from different locations can show whether the difference is within the active layer with particle-to-particle contact. The electronic conductivity of the active layer delaminated from the current collector at different locations is shown in Fig. 4.14c. There was no significant difference in electronic conductivity at different locations, showing that dependence of the contact loss on the location should be related to the region between the current collector and the active layer. It can thus be concluded that the large impedance at the outer radius of curvature in the curved region is due to a loss of contact between the active layer and the current collector. In order to determine whether or not this is caused by cycling, EIS tests were performed on the samples taken from the non-cycled cell at different locations, and the results of $2h_1$ are shown Fig. 4.14d. There was no significant effect of the location, revealing that the effect is a consequence of the cycling in combination with curvature. This study showed that cycling a prismatic cell leads to a significant loss of contact and increase in the impedance at the outer radius of curvature of the jellyroll in the curved region compared to the other locations, i.e. the inner radius of curvature or flat regions. This can partly explain the discrepancy in the loss of active NMC material between that calculated from the full cell and

the measured values from small samples taken from the jellyroll in the post-mortem analysis described in section 4.1.3.

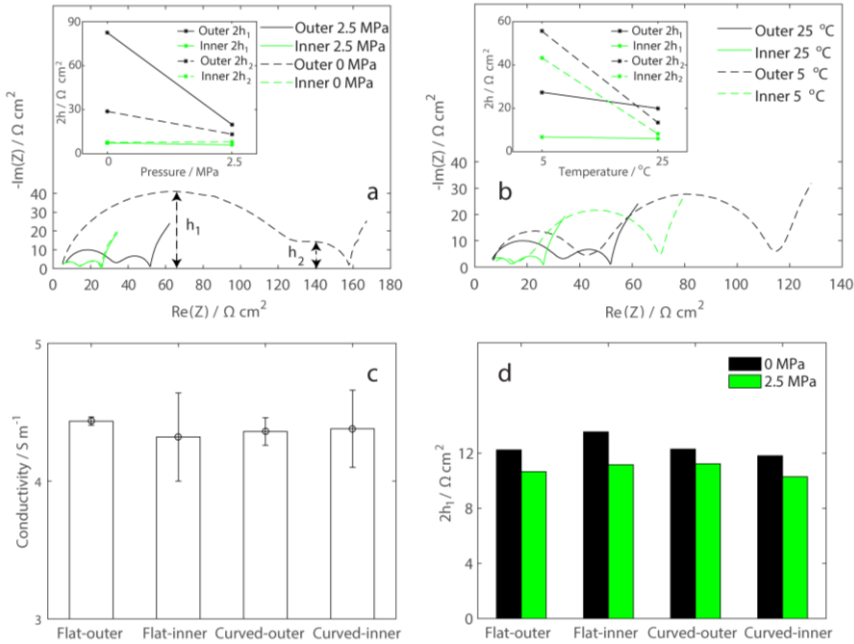


Fig. 4.14. EIS of the samples taken from the curved locations a) as a function of external compression b) as a function of temperature (insets show the diameter of the high frequency semi-circle ($2h_1$) and the mid-frequency semi-circle ($2h_2$)). c) Four-point probe electronic conductivity of active layer coatings taken from different locations. d) Variation in $2h_1$ with external compression at 25 °C for samples from the calendar-aged cell. Samples in a-d were taken from locations toward the cell skin.

4.3.2 Effects of current distribution

4.3.2.1 Initial performance

Unevenly distributed compression pressure and temperature can exist across the jellyrolls of a large-format cell or among cells connected in parallel in a battery module/pack. This can lead to a spatially non-uniform impedance and to the development of an uneven current distribution during battery operation. For instance, Fig. 4.15a shows the cell impedance at

different temperatures, where the impedance decreases at the higher temperature. Since the current is inversely proportional to impedance, such an uneven temperature distribution will lead to uneven currents during operation. The corresponding current distribution for three cells at 32, 36, or 40 °C and connected in parallel is shown in Fig. 4.15 (b, c) during charging at 1C and 3C rates, respectively. During 1C charging, an uneven current distribution is mainly seen for about the first 6 minutes, after which the current distribution becomes more or less uniform, even though a small reversal of the current distribution is seen towards the end of charging. Fig. 4.15 c. shows the current distribution during charging at 3C in a shorter SOC range, where the uneven current distribution is wider than at 1C. The high charging rate increases the difference between the currents passing through each cell at the beginning of charging in absolute terms and narrowing the SOC range stops the charging before the self-balancing occurs, resulting in a more uneven current distribution compared to the 1C charging in a narrower SOC range. High charging rate over a narrower SOC range thus widens the uneven current distribution caused by an uneven temperature distribution.

An uneven temperature distribution also affects the performance of a cell or a module/pack as a whole. Fig. 4.16 compares the impedance of two groups of cells: one group consisting of three cells at 32, 36, or 40 °C connected in parallel, and a second group with all three cells at 36 °C connected in parallel. It can be seen that the impedance with the uneven temperature distribution is similar to that with the even temperature distribution at the volume average value. This can be explained by the near linearity of the change of the real impedance at 10 mHz frequency with temperature above room temperature shown in the inset of Fig. 4.16. The impedances of the parallel connected cells with the even temperature distribution (R_e) and with the uneven temperature distribution (R_u) are described in terms the slope of the linear change in the impedance with the temperature (m) and the cell impedance at 36 °C (R_2) by Equations 4.1 and 4.2.

$$R_e = \frac{R_2}{3} \quad (4.1)$$

$$R_u = \frac{R_2^3 - 16m}{3R^2 - 16m} \quad (4.2)$$

If the slope m is small, the impedance at the uneven temperature distribution should be close to that of the even temperature distribution. This effect would be different at a cold average temperature where the change in impedance, especially the charge transfer resistance, with temperature is greater and highly non-linear. Troxler et al. [67] reported that a temperature gradient across a cell leads to a decrease in the cell impedance compared to that of the theoretical average temperature of the gradient.

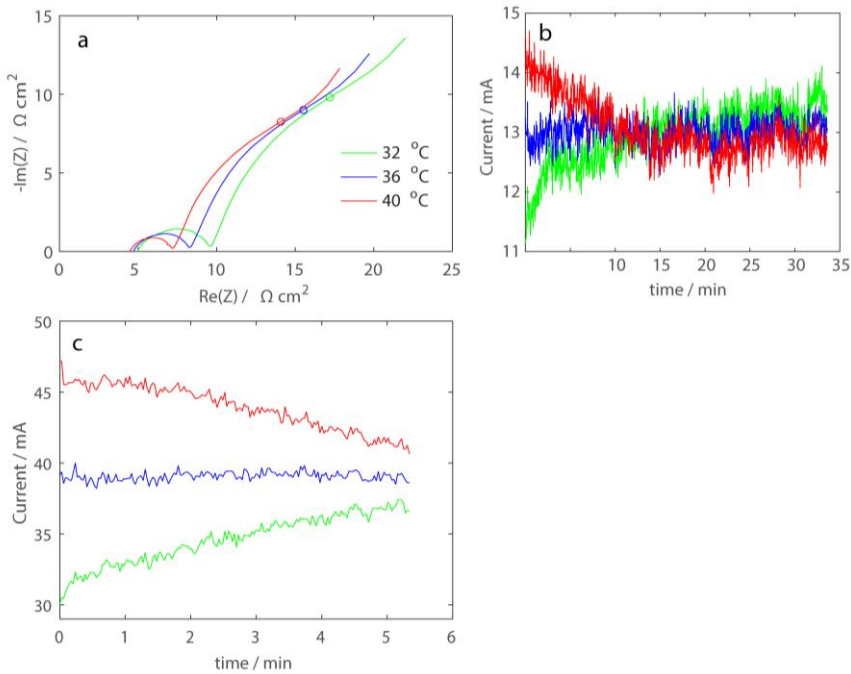


Fig. 4.15. a) Impedance in Nyquist plot as a function of temperature for a fresh cell. The corresponding current distribution in cells connected in parallel at b) 1C charging between 3.445 – 4.1 V, and c) 3C charging between 3.545 – 4.0 V. [o in (a) represent 10 mHz frequency].

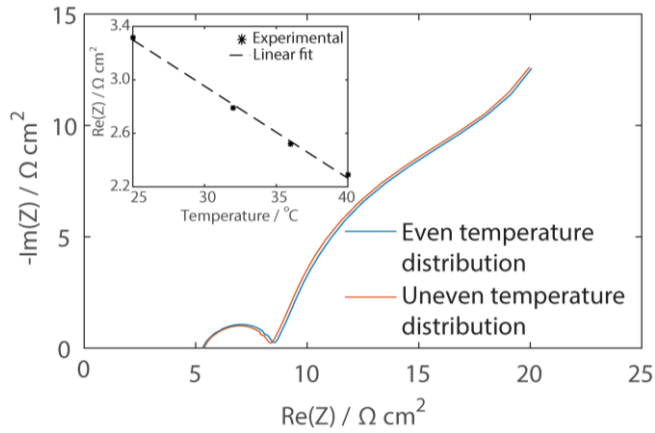


Fig. 4.16. Electrochemical impedance spectroscopy in Nyquist plot for a parallel group of cells tested at uniform (all at 36 °C) and non-uniform temperature (32, 36, 40 °C). (Inset: Impedance (Re(Z)) at 10 mHz frequency at the given temperature values.)

4.3.2.2 Cycling

The uneven current distribution induced by an uneven distribution of compression pressure or temperature could lead to non-uniform local ageing and accelerate the global ageing of the battery as a whole. This effect can be studied by coupling controlled cells at different temperatures and pressures in parallel. The capacity fade in the presence of compression pressure distribution is shown in Fig. 4.17, where the cell subjected to 0.66 MPa and coupled to the cell subjected to 1.32 MPa (Group 1) showed a capacity fade similar to that of the reference coupled cells both at 0.66 MPa and with no current distribution (Group 2). This indicates that the distribution of current between the cells does not accelerate battery ageing. If the current distribution affected the battery ageing, the cell subjected to 0.66 MPa pressure in group 1 would show a capacity loss different from that of the two cells in group 2.

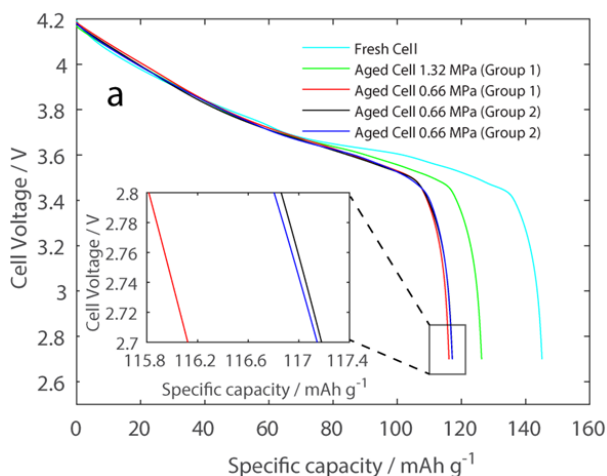


Fig. 4.17 Specific capacity of cells cycled in two groups connected in parallel at the end of life. (Group 1: cell at 1.32 MPa connected in parallel with a cell at 0.66 MPa; Group 2: two cells each at 0.66 MPa connected in parallel.)

Fig. 4.18 shows the capacity fade of a parallel connected group of cells with different temperatures (32, 36, and 40 °C) and cycled at 1C charge-discharge rate, and of non-coupled single cells cycled at the same charge-discharge rate and temperatures. The capacity fade of the parallel connected group was almost the same as that of the single cell cycled at 36 °C (Fig. 4.18a), and the C/25 capacity (Fig. 4.18b) of cells in the parallel group measured individually as single cells at the EOL had values similar to that of cells cycled as single cells at the corresponding temperatures. This shows that an uneven temperature distribution which induces only a moderately uneven current distribution does not accelerate the global battery ageing compared to the volume-averaged mean uniform temperature. This conclusion is supported by the modeling work of Filkernstein et al. [68] who reported that the capacity fade of a cell under a thermal gradient is similar to that of a cell cycled in the same manner but at the volume averaged uniform temperature. The data for the single cells shows that the difference in ageing between 32 and 36 °C was lower than that between 36 and 40 °C for the same 4 °C difference in temperature. This indicates that local ageing difference in an uneven temperature distribution depends not only on the magnitude of the temperature difference but also on the average temperature at which the difference exist.

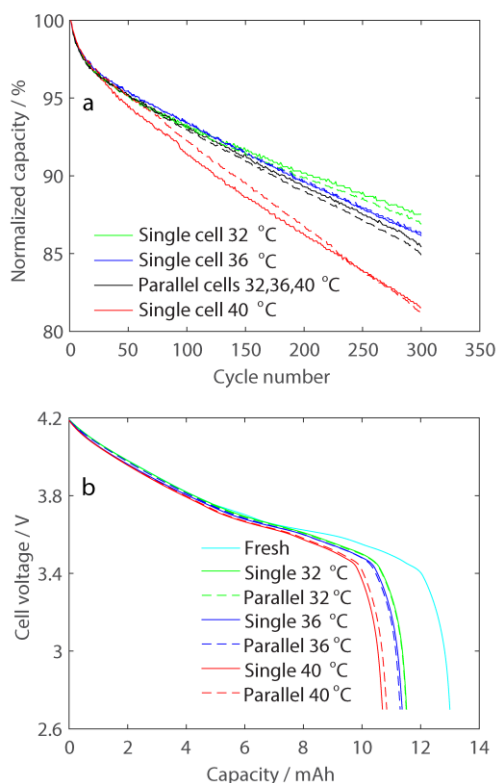


Fig. 4.18. a) Normalized discharge capacity as a function of cycle number during 1C charge-discharge cycling between 3.445 and 4.1 V for cells connected in parallel with temperature distribution (32, 36, and 40 °C) and for single cells cycled at the same temperatures. (Dotted lines are for the duplicate tests). b) C/25 discharge capacity at EOL, all measured independently as single cells. (The cycling voltage range, 3.445 – 4.1 V, corresponds to 11 – 94 % SOC based on the C/25 cell discharge capacity).

Fig. 4.19a shows the normalized discharge capacity in the case of 3C charge-discharge cycling, where the capacity fade of the cell group connected in parallel (32, 36, and 40 °C) was similar to that of the single cell cycled at the maximum temperature (40 °C). A comparison of the C/25 discharge capacities of the cycled cells at the EOL in Fig. 4.19b shows the capacity of the cell cycled at 40 °C in the parallel cell group was lower than that of the single cell at the same temperature by about 4.7%. The opposite was true for the cells cycled at 32 °C, where the cell in the parallel connection showed a capacity of 2.4 % greater than that of the corresponding single cell. The

difference in the capacity at the EOL is most likely due to the different current experienced by a cell when it is cycled in a parallel connection or as a single cell. The cells cycled at 32 and 40 °C experienced smaller and larger currents respectively when they were cycled in parallel rather than as single cells. The parallel connection seems to have a greater impact at 40 °C, probably because of a greater sensitivity of ageing to current above 3C for this type of cell.

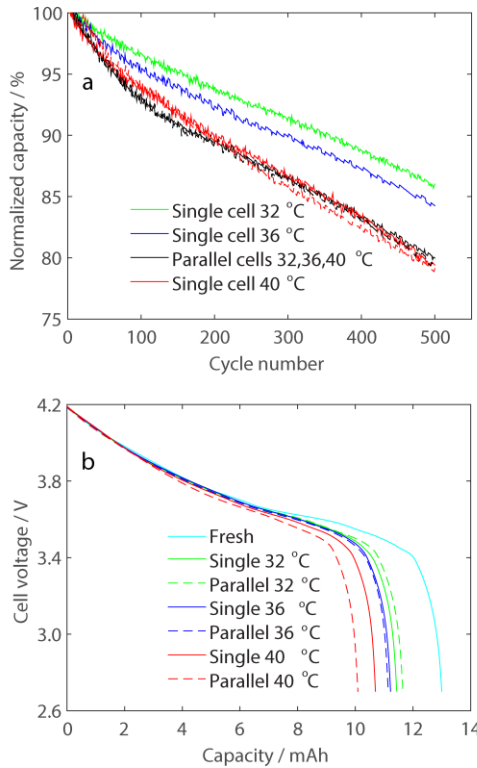


Fig. 4.19. a) Normalized discharge capacity as a function of cycle number during 3C charge-discharge cycling between 3.545 and 4.0 V for cells connected in parallel with a temperature distribution (32, 36, and 40 °C) and for single cells cycled at the same temperatures (Duplicate tests are performed for the parallel connected cell group and the single cell at 40 °C). b) C/25 discharge capacity at the EOL, measured independently as single cells. (The cycling voltage range, 3.545 – 4.0 V, corresponds to 22 – 86 % SOC based on the C/25 cell discharge capacity).

The result that cycling a battery under a high charge-discharge rate in a narrow SOC range caused faster ageing of the battery due to the effect of an uneven temperature distribution has an implication for the ageing of lithium-ion batteries used in the hybrid electric vehicles (HEVs). HEV batteries commonly operate at high charge and discharge rate in a narrow SOC range, hence, are more susceptible to accelerated ageing caused by the uneven temperature distribution.

In conclusion, we have seen that neither compression pressure distribution (0.66 and 1.32 MPa) at a 3C charge-discharge cycling nor temperature distribution (32, 36, and 40 °C) at a 1C charge-discharge cycling accelerated the global battery ageing, since the current distribution was narrow over the cycling period. On the other hand, when the current distribution was widened by increasing the charge-discharge rate and cycling in a narrower SOC range, the current distribution did indeed accelerate the global battery ageing. The ageing with the uneven temperature distribution of cells connected in parallel was similar to that of the single cell at the maximum temperature of the distribution. We can thus conclude that an uneven current distribution can accelerate the global battery ageing if its magnitude is sufficiently large.

5 Conclusions and outlook

The aim of the work reported in this thesis has been to investigate the effects of charging rate and protocol, external compression, and inhomogeneities on lithium-ion battery ageing under fast charging conditions. Top-down and bottom-up approaches were used in the investigation. The performance of large-format prismatic and cylindrical cells during cycling were tested at different charging rates and analyzed for local variations by post-mortem analysis. Small single-layer pouch cells that mimic different locations of a large format cell or their parallel connection were used to understand cycling performance and inhomogeneity on a larger scale in a controlled environment.

The effect of charging rate on lithium-ion battery ageing was characterized in a 25 Ah prismatic automotive cell at charging rates of 1C to 4C. Fast charging at a high rate, 3C and higher, accelerates battery ageing. The mechanisms that limit the battery life are associated with lithium plating and excessive gas evolution. Particle crack often associated with fast charging is observed irrespective of the charging rate and is not a mechanism that limits the fast charging capability in terms of the battery life.

At 2C and lower charging rates, tested on the prismatic and 1.5 Ah cylindrical cells, the cell ageing was observed to be less sensitive to charging rate and instead dominated by other factors such as the state of charge cycling window. Charging above ~80% SOC degrades the battery more than the charging rate. The lower sensitivity of battery ageing to charging rate at a rate of 2C and below is applicable only to single cell testing. This may not be the case in EV applications where multiple cells connected in series and in parallel are used. In such cases, thermal issues come into play and the rise in temperature induced by a higher charging rate can change the ageing.

In all the cases studied, the loss of lithium inventory is the limiting mode of ageing that determines the available cell capacity. Even if the losses of active electrode materials occur, they do not affect the capacity.

Ageing analyses results can be different between the full cell and the electrode samples harvested therein in the post-mortem analysis. The trend of impedance rise with cycling as a function of charging rate in the prismatic cells was different from the trend observed during measurement on the electrode samples. Additionally, the active mass loss was different between that calculated from the voltage fitting in the prismatic cell and that measured in the electrode samples. While post-mortem analysis is important to get detailed ageing information, some ageing mechanisms such as ion transport restriction between the jellyrolls and separator or contact loss at the characteristic locations that cause the difference may be overlooked by testing small samples taken from opened cells either due to the difficulty to measure or the sampling bias. Non-destructive analysis techniques such as cell voltage fitting should be used as a complementary technique in such cases in order to understand battery ageing mechanisms better.

The shift from the LFP to NMC-based commercial lithium-ion batteries also shifts the focus of ageing from only graphite to both the positive and the negative electrodes. The NMC electrode contributes equally or more than the graphite electrode to the cell degradation, especially to increase in the cell impedance.

Effects of external compression pressure on the performance and ageing of lithium-ion batteries were tested in a single-layer model pouch cell. An optimum compression pressure of around 1.3 MPa can extend battery life by reducing the cyclable lithium loss. The presence of an optimum pressure can explain some of the discrepancies reported in the literature regarding the trend of ageing along the length of the jelly-roll, between the core and the skin, of large-format cells.

Lithium-ion batteries age non-uniformly. The inhomogeneous ageing induced by the geometric design of a prismatic cell during cycling was studied by taking samples from the curved and flat regions of the jellyroll and making electrochemical impedance spectroscopy studies with varying external compression loads and temperatures. The geometric design of a prismatic cell is a disadvantage from the point of view of battery durability. The curvature regions at the outer radius of curvature of the jellyroll are

sensitive to a loss of contact between the current collector and the active electrode coating. The sensitivity is greatest towards the core along the length of a jellyroll. The bending stress at the outer curvature leads to the loss of contact when the battery is cycled for a long time. Cylindrical cell, which is geometrically compact, and pouch cell which has no jellyroll curvature could have a better performance in this regard.

Unfavorable current distribution due to an uneven temperature distribution accelerates the global battery ageing. The effect of an uneven current distribution is significant when cycling at a high charge-discharge rate over a narrow SOC range. Lithium-ion batteries used in hybrid vehicles, being used at a high charge-discharge rate in a narrow SOC range, are susceptible to faster battery ageing caused by uneven temperature or pressure induced current distribution.

Future work should consider a mechanistic study to examine how the optimum pressure reduces the cyclable lithium loss and how external compression affects the charge transfer and mass transport properties of a lithium-ion battery. Another interesting study could be an investigation of the coupled effect of bending stress and diffusion-induced stress at the curvature regions of a prismatic cell using a physical model that couples electrochemistry and mechanics.

6 Acknowledgements

To the Swedish energy agency for providing the financial support.

To my supervisors, Rakel Wreland Lindström (Associate Professor) and Göran Lindbergh (Professor), for giving me the opportunity to work in this field of study, and for their scientific discussions, guidance, and patience throughout my PhD study.

To Matilda Klett (Scania CV AB) for the mentoring, scientific discussions, guidance, and co-supervision.

To Pontus Svens (Scania CV AB) for all the help and scientific discussions, and for introducing me to the online battery diagnostics. To Mårten Behm for the all the help during the initial period my PhD study.

To all colleagues with whom I have collaborated in the “fast charging network”. Thank you for the smooth collaboration and wonderful scientific discussions. Time well spent!

To all my colleagues at Applied Electrochemistry. Thank you! You made my stay feel like home. Special thanks to Hyeyun Kim for all the fun moments.

To my former office mate and close friend, Huiran Lu. I miss those years together in the office!

To my family. Etu, Ababa, Jems,...; thank you for all your support, sacrifices, and endless love! Abi (Kedir Shewmolo); thank you for all the motivation, counseling, and inspiration since my childhood. My sweetheart wife, Ferhan Kedir; thank you for all your love, support, patience, and advice. Lucky me to share my life with you! Thank you all the rest of my family. You are the source of my happiness.

To all my friends in the Ethiopian Negashi community. Thank you!
የአሊህ ኢትዮጵያችንን አንተው ጠብቅልን!

7 References

- [1] A. Yoshino, *Angewandte Chemie International Edition*, 51 (2012) 5798-5800.
- [2] Z. Ogumi, R. Kostecki, D. Guyomard, M. Inaba, *The Electrochemical Society Interface*, 25 (2016) 65.
- [3] S. Pacala, R. Socolow, *Science*, 305 (2004) 968-972.
- [4] J.M. Tarascon, M. Armand, *Nature*, 414 (2001) 359-367.
- [5] U.d.o.e.o.o.e.e.a.r. energy, in, US department of energy office of energy efficiency and renewable energy, 2018, pp. All-Electric Vehicles.
- [6] A.C. Jussani, J.T.C. Wright, U. Ibusuki, *RAI Revista de Administração e Inovação*, 14 (2017) 333-338.
- [7] C. Michelbacher, S. Ahmed, I. Bloom, A. Burnham, B. Carlson, F. Dias, E.J. Dufek, A.N. Jansen, M. Keyser, A. Markel, A. Meintz, M. Mohanpurkar, A. Pesaran, D. Scofield, M. Shirk, T. Stephens, T. Tanim, R. Vijayagopal, J. Zhang, *Journal of Power Sources*, 367 (2017) 214-215.
- [8] S. Ahmed, I. Bloom, A.N. Jansen, T. Tanim, E.J. Dufek, A. Pesaran, A. Burnham, R.B. Carlson, F. Dias, K. Hardy, M. Keyser, C. Kreuzer, A. Markel, A. Meintz, C. Michelbacher, M. Mohanpurkar, P.A. Nelson, D.C. Robertson, D. Scofield, M. Shirk, T. Stephens, R. Vijayagopal, J. Zhang, *Journal of Power Sources*, 367 (2017) 250-262.
- [9] M. Keyser, A. Pesaran, Q. Li, S. Santhanagopalan, K. Smith, E. Wood, S. Ahmed, I. Bloom, E. Dufek, M. Shirk, A. Meintz, C. Kreuzer, C. Michelbacher, A. Burnham, T. Stephens, J. Francfort, B. Carlson, J. Zhang, R. Vijayagopal, K. Hardy, F. Dias, M. Mohanpurkar, D. Scofield, A.N. Jansen, T. Tanim, A. Markel, *Journal of Power Sources*, 367 (2017) 228-236.
- [10] J. Vetter, P. Novák, M.R. Wagner, C. Veit, K.C. Möller, J.O. Besenhard, M. Winter, M. Wohlfahrt-Mehrens, C. Vogler, A. Hammouche, *Journal of Power Sources*, 147 (2005) 269-281.
- [11] T. Waldmann, S. Gorse, T. Samtleben, G. Schneider, V. Knoblauch, M. Wohlfahrt-Mehrens, *Journal of The Electrochemical Society*, 161 (2014) A1742-A1747.
- [12] A. Barré, B. Deguilhem, S. Grolleau, M. Gérard, F. Suard, D. Riu, *Journal of Power Sources*, 241 (2013) 680-689.
- [13] F. Leng, C.M. Tan, M. Pecht, *Scientific Reports*, 5 (2015) 12967.
- [14] V. Agubra, J. Fergus, *Materials*, 6 (2013) 1310.
- [15] M. Broussely, P. Biensan, F. Bonhomme, P. Blanchard, S. Herreyre, K. Nechev, R.J. Staniewicz, *Journal of Power Sources*, 146 (2005) 90-96.
- [16] M. Wohlfahrt-Mehrens, C. Vogler, J. Garche, *Journal of Power Sources*, 127 (2004) 58-64.

- [17] R. Hausbrand, G. Cherkashinin, H. Ehrenberg, M. Gröting, K. Albe, C. Hess, W. Jaegermann, *Materials Science and Engineering: B*, 192 (2015) 3-25.
- [18] L. Lu, X. Han, J. Li, J. Hua, M. Ouyang, *Journal of Power Sources*, 226 (2013) 272-288.
- [19] F. An, L. Chen, J. Huang, J. Zhang, P. Li, *Scientific Reports*, 6 (2016) 35051.
- [20] W. Shi, X. Hu, C. Jin, J. Jiang, Y. Zhang, T. Yip, *Journal of Power Sources*, 313 (2016) 198-204.
- [21] N. Yang, X. Zhang, B. Shang, G. Li, *Journal of Power Sources*, 306 (2016) 733-741.
- [22] T. Bruen, J. Marco, *Journal of Power Sources*, 310 (2016) 91-101.
- [23] C. Pastor-Fernández, T. Bruen, W.D. Widanage, M.A. Gama-Valdez, J. Marco, *Journal of Power Sources*, 329 (2016) 574-585.
- [24] X. Gong, R. Xiong, C.C. Mi, *IEEE Transactions on Industry Applications*, 51 (2015) 1872-1879.
- [25] S. Paul, C. Diegelmann, H. Kabza, W. Tillmetz, *Journal of Power Sources*, 239 (2013) 642-650.
- [26] M. Dubarry, N. Vuillaume, Y. Liaw Bor, *International Journal of Energy Research*, 34 (2010) 216-231.
- [27] N. Nitta, F. Wu, J.T. Lee, G. Yushin, *Materials Today*, 18 (2015) 252-264.
- [28] F. Schipper, P. Nayak, E. Erickson, S. Amalraj, O. Srur-Lavi, T. Penki, M. Talianker, J. Grinblat, H. Sclar, O. Breuer, C. Julien, N. Munichandraiah, D. Kovacheva, M. Dixit, D. Major, B. Markovsky, D. Aurbach, *Inorganics*, 5 (2017) 32.
- [29] G.E. Blomgren, *Journal of The Electrochemical Society*, 164 (2017) A5019-A5025.
- [30] L.H. Saw, Y. Ye, A.A.O. Tay, *Journal of Cleaner Production*, 113 (2016) 1032-1045.
- [31] D. Andrea, *Battery Management Systems for Large Lithium Ion Battery Packs*, 2010.
- [32] Nrel, A. Pesaran, G.H. Kim, M. Keyser, *Integration Issues of Cells into Battery Packs for Plug-In and Hybrid Electric Vehicles*, 2009.
- [33] W.A.v. Schalkwijk, B. Scrosati, *Advances in Lithium-Ion Batteries*, 2002.
- [34] E. Maiser, *AIP Conference Proceedings*, 1597 (2014) 204-218.
- [35] T.M. Bandhauer, S. Garimella, T.F. Fuller, *Journal of The Electrochemical Society*, 158 (2011) R1-R25.
- [36] H. Lundgren, P. Svens, H. Ekström, C. Tengstedt, J. Lindström, M. Behm, G. Lindbergh, *Journal of The Electrochemical Society*, 163 (2016) A309-A317.
- [37] G. Zhang, L. Cao, S. Ge, C.-Y. Wang, C.E. Shaffer, C.D. Rahn, *Journal of The Electrochemical Society*, 161 (2014) A1499-A1507.
- [38] C. Veth, D. Dragicevic, C. Merten, *Journal of Power Sources*, 267 (2014) 760-769.
- [39] T. Grandjean, A. Barai, E. Hosseinzadeh, Y. Guo, A. McGordon, J. Marco, *Journal of Power Sources*, 359 (2017) 215-225.

- [40] L. Zheng, B. Wu, G. Qing Xu, Investigation of the Temperature Distribution in the Lithium-Ion Battery for Pure Electric Vehicles, 2012.
- [41] M.P. Klein, J.W. Park, Journal of The Electrochemical Society, 164 (2017) A1893-A1906.
- [42] T. Wang, K.J. Tseng, J. Zhao, Z. Wei, Applied Energy, 134 (2014) 229-238.
- [43] J. Yi, B. Koo, C. Shin, Energies, 7 (2014) 7586.
- [44] T.R. Tanim, M.G. Shirk, R.L. Bewley, E.J. Dufek, B.Y. Liaw, Journal of Power Sources, 381 (2018) 56-65.
- [45] J. Cannarella, C.B. Arnold, Journal of Power Sources, 245 (2014) 745-751.
- [46] Y. Zhao, Y. Patel, I.A. Hunt, K.M. Kareh, A.A. Holland, C. Korte, J.P. Dear, Y. Yue, G.J. Offer, Journal of Energy Storage, 13 (2017) 296-303.
- [47] R. Gogoana, M.B. Pinson, M.Z. Bazant, S.E. Sarma, Journal of Power Sources, 252 (2014) 8-13.
- [48] M. Klett, R. Eriksson, J. Groot, P. Svens, K. Ciosek Högström, R.W. Lindström, H. Berg, T. Gustafson, G. Lindbergh, K. Edström, Journal of Power Sources, 257 (2014) 126-137.
- [49] C. Lin, A. Tang, H. Mu, W. Wang, C. Wang, Journal of Chemistry, 2015 (2015) 11.
- [50] E. Peled, S. Menkin, Journal of The Electrochemical Society, 164 (2017) A1703-A1719.
- [51] S.J. An, J. Li, C. Daniel, D. Mohanty, S. Nagpure, D.L. Wood, Carbon, 105 (2016) 52-76.
- [52] B. Michalak, H. Sommer, D. Mannes, A. Kaestner, T. Brezesinski, J. Janek, Scientific Reports, 5 (2015) 15627.
- [53] W. Kong, H. Li, X. Huang, L. Chen, Journal of Power Sources, 142 (2005) 285-291.
- [54] C. Botsford, A. Szczepanek, in: EVS24, Stavanger, Norway, 2009.
- [55] Q. Liu, C. Du, B. Shen, P. Zuo, X. Cheng, Y. Ma, G. Yin, Y. Gao, RSC Advances, 6 (2016) 88683-88700.
- [56] T. Waldmann, B.I. Hogg, M. Kasper, S. Grolleau, C.G. Couceiro, K. Trad, B.P. Matadi, M. Wohlfahrt-Mehrens, Journal of the Electrochemical Society, 163 (2016) A1232-A1238.
- [57] K.G. Gallagher, S.E. Trask, C. Bauer, T. Woehrle, S.F. Lux, M. Tschech, P. Lamp, B.J. Polzin, S. Ha, B. Long, Q. Wu, W. Lu, D.W. Dees, A.N. Jansen, Journal of The Electrochemical Society, 163 (2016) A138-A149.
- [58] P. Arora, M. Doyle, R.E. White, Journal of The Electrochemical Society, 146 (1999) 3543-3553.
- [59] L. Somerville, J. Bareño, S. Trask, P. Jennings, A. McGordon, C. Lyness, I. Bloom, Journal of Power Sources, 335 (2016) 189-196.
- [60] K. Zhao, M. Pharr, J.J. Vlassak, Z. Suo, Journal of Applied Physics, 108 (2010) 073517.
- [61] T. Waldmann, M. Wilka, M. Kasper, M. Fleischhammer, M. Wohlfahrt-Mehrens, Journal of Power Sources, 262 (2014) 129-135.

- [62] T.C. Bach, S.F. Schuster, E. Fleder, J. Müller, M.J. Brand, H. Lorrmann, A. Jossen, G. Sextl, *Journal of Energy Storage*, 5 (2016) 212-223.
- [63] C. Peabody, C.B. Arnold, *Journal of Power Sources*, 196 (2011) 8147-8153.
- [64] D. Sauerteig, N. Hanselmann, A. Arzberger, H. Reinshagen, S. Ivanov, A. Bund, *Journal of Power Sources*, 378 (2018) 235-247.
- [65] R.S. Rubino, H. Gan, E.S. Takeuchi, *Journal of The Electrochemical Society*, 148 (2001) A1029-A1033.
- [66] M. Petzl, M. Kasper, M.A. Danzer, *Journal of Power Sources*, 275 (2015) 799-807.
- [67] Y. Troxler, B. Wu, M. Marinescu, V. Yufit, Y. Patel, A.J. Marquis, N.P. Brandon, G.J. Offer, *Journal of Power Sources*, 247 (2014) 1018-1025.
- [68] M. Fleckenstein, O. Bohlen, B. Bäker, *World Electric Vehicle Journal*, 5 (2012).
- [69] I.A. Hunt, Y. Zhao, Y. Patel, G.J. Offer, *Journal of The Electrochemical Society*, 163 (2016) A1846-A1852.
- [70] J. Cannarella, C.B. Arnold, *Journal of The Electrochemical Society*, 162 (2015) A1365-A1373.
- [71] I. Bloom, A.N. Jansen, D.P. Abraham, J. Knuth, S.A. Jones, V.S. Battaglia, G.L. Henriksen, *Journal of Power Sources*, 139 (2005) 295-303.
- [72] M. Dubarry, V. Svoboda, R. Hwu, B.Y. Liaw, *Electrochemical and Solid-State Letters*, 9 (2006) A454-A457.
- [73] B. Wu, V. Yufit, Y. Merla, R.F. Martinez-Botas, N.P. Brandon, G.J. Offer, *Journal of Power Sources*, 273 (2015) 495-501.
- [74] K. Honkura, H. Honbo, Y. Koishikawa, T. Horiba, *ECS Transactions*, 13 (2008) 61-73.
- [75] K. Honkura, T. Horiba, *Journal of Power Sources*, 264 (2014) 140-146.
- [76] S.F. Schuster, T. Bach, E. Fleder, J. Müller, M. Brand, G. Sextl, A. Jossen, *Journal of Energy Storage*, 1 (2015) 44-53.
- [77] Q. Zhang, R.E. White, *Journal of Power Sources*, 179 (2008) 793-798.
- [78] I. Bloom, B.G. Potter, C.S. Johnson, K.L. Gering, J.P. Christophersen, *Journal of Power Sources*, 155 (2006) 415-419.
- [79] B. Lunz, Z. Yan, J.B. Gerschler, D.U. Sauer, *Energy Policy*, 46 (2012) 511-519.
- [80] A.S. Mussa, M. Klett, M. Behm, G. Lindbergh, R.W. Lindström, *Journal of Energy Storage*, 13 (2017) 325-333.
- [81] K. Amine, J. Liu, I. Belharouak, *Electrochemistry Communications*, 7 (2005) 669-673.
- [82] E. Sarasketa-Zabala, F. Aguesse, I. Villarreal, L.M. Rodriguez-Martinez, C.M. López, P. Kubiak, *The Journal of Physical Chemistry C*, 119 (2015) 896-906.
- [83] P. Liu, J. Wang, J. Hicks-Garner, E. Sherman, S. Soukiazian, M. Verbrugge, H. Tataria, J. Musser, P. Finamore, *Journal of The Electrochemical Society*, 157 (2010) A499-A507.

- [84] R. Xu, K. Zhao, *Journal of Electrochemical Energy Conversion and Storage*, 13 (2016) 030803-030803-030809.
- [85] Y.S. Jung, A.S. Cavanagh, L.A. Riley, S.H. Kang, A.C. Dillon, M.D. Groner, S.M. George, S.H. Lee, *Advanced Materials*, 22 (2010) 2172-2176.
- [86] I.R.M. Kottegoda, Y. Kadoma, H. Ikuta, Y. Uchimoto, M. Wakihara, *Journal of The Electrochemical Society*, 152 (2005) A1595-A1599.
- [87] S.-S. Kim, Y. Kadoma, H. Ikuta, Y. Uchimoto, M. Wakihara, *Electrochemical and Solid-State Letters*, 4 (2001) A109-A112.
- [88] S.-E. Lee, E. Kim, J. Cho, *Electrochemical and Solid-State Letters*, 10 (2007) A1-A4.
- [89] D. Aurbach, M.D. Levi, E. Levi, H. Teller, B. Markovsky, G. Salitra, U. Heider, L. Heider, *Journal of The Electrochemical Society*, 145 (1998) 3024-3034.
- [90] H. Zheng, L. Tan, G. Liu, X. Song, V.S. Battaglia, *Journal of Power Sources*, 208 (2012) 52-57.
- [91] C. Lim, B. Yan, H. Kang, Z. Song, W.C. Lee, V. De Andrade, F. De Carlo, L. Yin, Y. Kim, L. Zhu, *Journal of Power Sources*, 328 (2016) 46-55.
- [92] T.G. Zavalis, M. Klett, M.H. Kjell, M. Behm, R.W. Lindström, G. Lindbergh, *Electrochimica Acta*, 110 (2013) 335-348.
- [93] A.-K. Hjelm, G. Lindbergh, *Electrochimica Acta*, 47 (2002) 1747-1759.